RSC Advances

PAPER

View Article Online
View Journal | View Issue

Cite this: *RSC Adv.*, 2026, **16**, 25269

Synergistic effects of nitrogen doping in waste-fruit peel–derived activated carbons for supercapacitors and water treatment

Vianney Kitenge, *[ab] Ndeye Fatou Diop,[a] Souleyman Thior,[a] Adama Fall,[b] Kabir Otun,[a] Gift Rutavi,[a] Itani Madiba,[b] Ncholu Manyala,[a] Mohamed Chaker[c] and Maaza Malik[b]

Developing sustainable carbon materials from agricultural waste offers promising solutions to both energy-storage and water-treatment challenges. This study reports the synthesis of a nitrogen-doped Tondolo-derived activated carbon (N-TAC), an underexplored African wetland sedge whose fibrous morphology directs pore architecture. Rather than conventional dry mixing, K_2CO_3 and urea were co-dissolved and intimately blended with the finely reduced Tondolo precursor. This reagent-level homogeneity enabled a single pyrolysis at 700 °C in which carbonisation, chemical activation, and nitrogen doping proceeded concurrently. The N-TAC Near-surface nitrogen functionalities (pyridinic, pyrrolic, and graphitic) proved decisive in enhancing both electrochemical and adsorptive performance. Three-electrode characterization in 1 M $NaNO_3$ revealed coexisting EDLC and pseudocapacitive mechanisms, with a low ESR of 2.05 Ω and relaxation time constant of 0.87 s confirming rapid ion diffusion kinetics. Trasatti deconvolution and Dunn's method reveal that pyridinic and pyrrolic sites selectively amplify pseudocapacitive contributions (63–71%) in the positive potential window, a window-dependent asymmetry not previously reported for neutral-electrolyte biomass carbons. The assembled symmetric device delivered 12.1 Wh kg^{-1} with 94% capacitance retention after 10 000 cycles. For water remediation, N-TAC achieved 99.9% methylene blue removal at 50 ppm with an adsorption capacity of 557.6 mg g^{-1}, governed by chemisorption *via* electrostatic and π–π interactions, best described by pseudo-second-order kinetics ($R^2 = 0.97$) and the Temkin isotherm ($R^2 = 0.958$). These results position N-TAC as a competitive sustainable material at the water–energy nexus, with future perspectives including binder-free electrode fabrication, electrochemical degradation coupling, and regenerable architectures for long-term sustainability.

Received 13th March 2026
Accepted 4th May 2026

DOI: 10.1039/d6ra02137a

rsc.li/rsc-advances

1. Introduction

The development of multifunctional carbon materials addresses critical challenges in energy storage and water remediation.[1,2] Supercapacitors require electrode materials with high specific surface area, tunable porosity, and heteroatom doping to enhance both electrical double-layer capacitance and pseudo capacitance.[1,3–5] Simultaneously, water contamination by persistent organic pollutants such as methylene blue, a cationic dye widely used in textiles and known for its stability and toxicity, demands efficient adsorbents with high surface area and favourable surface chemistry for electrostatic and π–π interactions.[6]

Agricultural waste-derived activated carbons offer a sustainable approach to both applications, converting biomass into high-value functional materials.[7,8] Activated carbon (AC) can be considered a vital solution for sustainable water and energy management.[9,10] The material's intricate three-dimensional network of interconnected pores creates an exceptional platform for pollutant capture, molecular separation, and water purification.[11] This structural configuration maximises opportunities for surface interactions between contaminants and active sites, establishing the material as particularly valuable for deployment in continuous-flow adsorption systems for water remediation.[12] AC versatility makes it also suitable for energy storage systems, particularly as electrode material in electric double-layer capacitors (EDLCs), which store charges through rapid electrostatic adsorption of electrolyte ions, forming electric double layers, and enabling swift energy storage and

[a]*Department of Physics, SARChI Chair in Nanomaterials for Energy Storage and Water Purification Applications, University of Pretoria, Pretoria 0002, South Africa. E-mail: Vianney.kitenge@up.ac.za; Ncholu.manyala@up.ac.za*

[b]*UNESCO-UNISA Africa Chair in Nanosciences & Nanotechnology Laboratories, College of Graduate Studies, University of South Africa, Muckleneuk Ridge, P.O. Box 392, Pretoria 0003, South Africa*

[c]*Institut National de La Recherche Scientifique Centre – Énergie Matériaux Télécommunications, 1650, Boul. Lionel Boulet, Varennes, Québec J3X 1S2, Canada*

release.[13,14] The efficiency of activated carbon in dye adsorption and EDLC applications is significantly influenced by its pore size distribution and surface chemistry.[15] AC with optimal porous structures, comprising micropores and mesopores, exhibits enhanced physicochemical properties.[16]

Various organic waste materials, rich in carbon, have been successfully converted into activated carbon including coconut shells, fruit peels (banana,[17] orange,[18] avocado,[19] and mangosteen[14,20,21]), peanut shells,[22] wallnuts,[23] Amarula seed husks,[10] cow heel,[24] human hair,[25] and so on. These works established that biomass composition, particularly lignocellulosic content, directly influences the porosity and surface chemistry of resulting activated carbons.[26,27] Despite this diversity of precursors, most reported agricultural waste-derived carbons originate from widely cultivated, globally abundant crops. Carbon precursors derived from regionally endemic or underexplored fruit species remain significantly underrepresented in the literature, representing an untapped opportunity to valorise locally available waste streams while tailoring carbon properties through precursor-specific lignocellulosic compositions.

Surface modification techniques, such as functionalization and doping with heteroatoms, further improve electrochemical performance by enhancing wettability, electrical conductivity, and introducing redox-active sites.[14,28] Notably, heteroatom doping, particularly with nitrogen, creates beneficial defects, increases electronegativity, and boosts charge–discharge, self-discharge, and capacitance properties.[29] Additionally, the generated nitrogen atoms create various functional groups that serve as active sites with localized negative charge, promoting strong electrostatic interactions with cationic pollutants like methylene blue.[30,31] The combined effect of these chemical and physical modifications results in substantially higher adsorption capacities, faster kinetics, and improved selectivity.[32] Furthermore, recent advances have shown that nitrogen doping *via* urea or melamine treatment enhances both electrochemical performance and adsorption capacity through the introduction of pseudocapacitive sites and electrostatic interactions. However, most reported synthesis protocols involve multi-step processes including pre-carbonisation followed by separate activation and heteroatom doping stages, increasing production time, energy consumption, and overall cost. In the present work, this limitation is addressed through a process-engineered single pyrolysis approach in which K_2CO_3 and urea are co-dissolved in water and combined with Tondolo biomass reduced to sub-5 μm particles by ball milling. The resulting reagent-level homogeneity ensures that carbonisation, chemical activation, and nitrogen doping proceed concurrently during a single pyrolysis, eliminating intermediate stages while maximising nitrogen incorporation and reagent–precursor contact during pore development.

Tondolo, a wild indigenous fruit tree native to sub-Saharan Africa, has recently been demonstrated as a viable nitrogen-doped activated carbon precursor with promising capacitive performance.[1] However, the mechanistic underpinning of its charge storage behavior, its practical device-level performance, and its potential for methylene blue remain unreported, representing significant knowledge gaps that limit the broader valorisation of this indigenous biomass. Building on this foundation, the novelty of the present work is threefold: (i) comprehensive mechanistic charge storage characterisation of N-TAC through power law analysis, Trasatti deconvolution, and Dunn's method, quantitatively establishing the pseudocapacitive nature and potential-dependent asymmetric behavior of the material in neutral aqueous electrolyte; (ii) fabrication and electrochemical evaluation of a symmetric N-TAC//N-TAC supercapacitor device operating at 1.7 V with full performance benchmarking; and (iii) introduction of N-TAC as a bifunctional material through comprehensive methylene blue adsorption studies encompassing kinetic and equilibrium isotherm analysis, establishing its dual applicability at the water–energy nexus.

2. Experimental

2.1 Material and synthesis

2.1.1 Synthesis of activated carbon derived from Tondolo peels. Aframomum alboviolaceum, commonly known as Tondolo, is a perennial herbaceous plant native to tropical Africa.[33] Characterized by its deep-creeping rhizomes, Tondolo produces sturdy stems reaching up to 3 meters in height and bears fruits at its base. Tondolo-derived activated carbon (TAC) was synthesized following our previously published method.[1] Briefly, Tondolo peels from Gambela market (DRC) were washed, dried (60 °C, 12 h), and milled. The crushed peels were mixed with K_2CO_3 (1 : 1 mass ratio) and deionized water, dried, then carbonized at 700 °C for 2 h under Argon flow. The material was acid-treated (3 M HCl, 5 h), washed to neutral pH, and dried to yield TAC.

2.1.2 Synthesis of nitrogen-doped activated carbon from Tondolo peels. Nitrogen-doped Tondolo-derived activated carbon (N-TAC) was synthesized *via* a process-engineered single pyrolysis approach designed to achieve reagent-level homogeneity between the precursor and chemical agents.[1,14] In brief, Tondolo peels were first subjected to ball milling until a particle size below 5 μm was obtained. K_2CO_3 and urea were co-dissolved in deionized water at a mass ratio of 1 : 1 : 1 with respect to the Tondolo biomass and the resulting solution was thoroughly combined with the milled peels. The mixture was dried to remove residual moisture prior to thermal treatment. The dried precursor was placed in a tube furnace at 700 °C for 2 h under argon flow, during which carbonisation, chemical activation by K_2CO_3, and nitrogen doping by urea decomposition proceeded concurrently. The material was subsequently acid-treated (3 M HCl, 5 h), washed to neutral pH, and dried to yield N-TAC.

2.2 Characterization

The materials textural properties were analysed with a NOVAtouch LX^2-Quanta Chrome pore size distribution and surface area analyzer (BET technique, P/P_0 = 0.05–0.95). Microscopy images were acquired using a Zeiss Ultra Plus 55 FE-SEM (2.0 kV). Raman spectroscopy was performed using a WITec Alpha 300 RAS+ (523 nm, 4 mW, 120 s). X-ray photoelectron

spectroscopy (XPS) measurements were conducted with a VG Escalab 220i-XL instrument (Al–K source, 0.6 eV).

2.3 Electrochemical measurements

Electrodes were prepared by mixing 80% active material, 10% polyvinylidene difluoride (PVDF), and 10% conductive carbon acetylene black. N-methyl-2-pyrrolidone (NMP) drops formed a slurry, which was pasted onto 1 cm^2 Ni-foam current collectors. The electrodes were dried at 60 °C for 12 hours. Active material mass loading ranged from 2.5 to 3 mg cm^{-2}. This mass loading range was selected based on previous studies that demonstrated optimal electrochemical performance through balanced ion transport and electronic conductivity.[9] Since the primary objective was to investigate nitrogen doping effects, maintaining consistent mass loading was essential to ensure reliable inter-sample comparisons and minimize mass-related variations in electrochemical measurements.

A Biologic VMP300 potentiostat with EC-Lab V11.33 software was used for two- and three-electrode analyses. The three-electrode setup consisted of a working electrode (synthesized material), a counter electrode (Glassy Carbon), and a reference electrode (Ag/AgCl). Measurements were conducted in 1 M $NaNo_3$ as the electrolyte at room temperature. CV analysis was performed against the Ag/AgCl reference electrode at multiple scan rates and working potentials (−0.9 to 0.0 V and 0.0 to 0.8 V). GCDs were performed at various specific currents within CV potential ranges. EIS measurements were taken at frequencies from 100 kHz to 10 mHz.

The specific capacitances (C_{sp}) from the discharge slope of the Galvanostatic Charge–Discharge (GCD) curves was determined using the following formula:[34]

$$C_{sp} = \frac{I\Delta t}{\Delta V m} \quad (1)$$

with m: the mass of the electrode; I: the applied current, Δt: the discharge time, and ΔV: the potential window.

Eqn (2) was used to estimate how much charge is stored on each electrode as follows:[35]

$$\frac{m_+}{m_-} = \frac{Q_{s-}}{Q_{s+}} \quad (2)$$

To ensures an optimal mass ratio between the two electrodes for balanced charge storage in the device, the mass balance was calculated using:[36]

$$C_{sp,+}\, m_+ \Delta V_+ = C_{sp,-}\, m_- \Delta V_- \quad (3)$$

where:$C_{sp,+}$ and $C_{sp,-}$ = specific capacitances of the positive and negative electrodes (F g^{-1}).m_+ and m_- = masses of the positive and negative electrodes (g).ΔV_+ and ΔV_- = potential windows of the positive and negative electrodes (V).

The specific capacitance (C_{single}) of a single electrode in the device was calculated using:[10]

$$C_{single(sp)} = \frac{2I\Delta t}{\Delta V \frac{M_t}{2}} = \frac{4I\Delta t}{\Delta V M_t} \quad (4)$$

where:$C_{single(sp)}$ = single-electrode specific capacitance (F g^{-1}).I = applied current (A).Δt = discharge time (s).ΔV = device voltage (V).M_t = total mass of both electrodes (g).

The device's specific energies (E_s) in joules per gram (Wh kg^{-1}) and their specific powers (P_s, w kg^{-1}) were determined using eqn (5) and (6) as follow:[9]

$$E_s = \frac{1}{2} C_{single(sp)} (\Delta V)^2 = \frac{1000 \times C_{single(sp)} \times (\Delta V)^2}{2 \times 4 \times 3600} \quad (5)$$

where, C_{single} = device single electrode capacitance, and

$$P_s = 3600 \times \frac{E_s}{\Delta t} \quad (6)$$

where, Δt = device's discharge time.

The coulombic efficiencies were obtained from the GCD curves *via* equation below:[20]

$$\varepsilon\% = \frac{\Delta t_{discharge}}{\Delta t_{charge}} \times 100 \quad (7)$$

2.4 Adsorption studies

Dye adsorption experiments were conducted to evaluate the purification capacity of the synthesized TAC and optimized N-TAC using various Methylene Blue solution concentrations.[30]

The adsorption efficiency of TAC *versus* N-TAC was evaluated using Methylene Blue removal from 60 ppm aqueous solutions. For dosage optimization, N-TAC was tested at three masses (10, 20, and 30 mg) to establish optimal removal parameters.

Batches of 10 mg N-TAC were dispersed in 50 mL Methylene Blue solutions (20–150 ppm) and agitated at 25 °C. UV-vis measurements were recorded at intervals from 0–60 minutes for kinetic analysis, with equilibrium values determined after 24 hours.

Dye concentrations were calculated from UV-vis absorbance using Beer's Law:[37]

$$A = \varepsilon b c \quad (8)$$

where A is absorbance, ε is molar absorptivity (7.4×10^4 L mol^{-1} cm^{-1}), b is path length (1 cm), and c is molar concentration. Molar concentrations were converted to mass concentrations (ppm) using:[23]

$$\text{Concentration (PPM)} = C\ (\text{mol}\ l^{-1}) \times \text{MW}\ (\text{g mol}^{-1}) \times 10^{-3} \quad (9)$$

The adsorption capacities at time t (q_t) were calculated using the following equations:[1]

$$q_t = \frac{C_0 - C_t}{m} \times V \quad (10)$$

where:q_t = adsorption capacity (mg g^{-1}).C_0 = concentration of methylene blue before adsorption time t (ppm).C_t = concentration of methylene blue at time t during adsorption (ppm).V = volume of methylene blue solution (L).m = mass of TAC/N-TAC (g).

The adsorption at equilibrium (after 24 hours) (q_e) was determined as follows:[1]

$$q_e = \frac{C_0 - C_e}{m} \times V \quad (11)$$

where:q_e = adsorption capacity at equilibrium (mg g^{-1}).C_0 = concentration of methylene blue before adsorption time t (ppm).C_e = concentration of methylene blue at equilibrium (ppm).V = volume of methylene blue solution (L).m = mass of N-TAC (g).

The methylene blue rate of removal efficiency (R = removal efficiency (%)) was determined as follows:[1]

$$R(\%) = \frac{C_0 - C_t}{C_0} \times 100 \quad (12)$$

2.5 Reproducibility

All experimental measurements were conducted in triplicate ($n \geq 3$). BET surface area measurements showed standard deviations below 3%, while electrochemical measurements demonstrated variations within ±5%. Cycled electrodes were recovered, rewashed, and reassembled into new cells, confirming performance retention within ±5%. Adsorption experiments yielded dye removal standard deviations below 2%. Multiple independent synthesis batches confirmed the robustness and scalability of the fabrication protocol, with all performance variations remaining within ±5%.

3. Results and discussion

3.1 Textural and morphological characterisation

The textural properties and morphology of TAC and N-TAC are illustrated in Fig. 1. Both materials exhibit Type IVa isotherms with H4 hysteresis loops (Fig. 1(a)), characteristic of micro–mesoporous carbons with slit-like pores. N-TAC displays significantly higher nitrogen uptake than TAC, corresponding to its enhanced surface area (3504.5 m^2 g^{-1} *versus* 2331.15 m^2 g^{-1}) and micropore volume (Table 1). This surface area enhancement is attributed to the role of urea-derived nitrogen species during thermal treatment: the decomposition of urea generates NH_3 and HNCO gases that act as additional *in situ* activation agents, etching the carbon framework and creating supplementary micropores beyond those generated by K_2CO_3 alone.[38,39] The concurrent nitrogen incorporation stabilizes newly formed pore walls through C–N bonding, preventing pore collapse during high-temperature activation and contributing to the significantly higher micropore volume of N-TAC (1.38 cc g^{-1}) compared to TAC (0.86 cc g^{-1}). The pore size distribution (Fig. 1(b)) confirms higher pore volume for N-TAC, while SEM micrographs (Fig. 1(a_1) and (a_2)) reveal a disordered porous

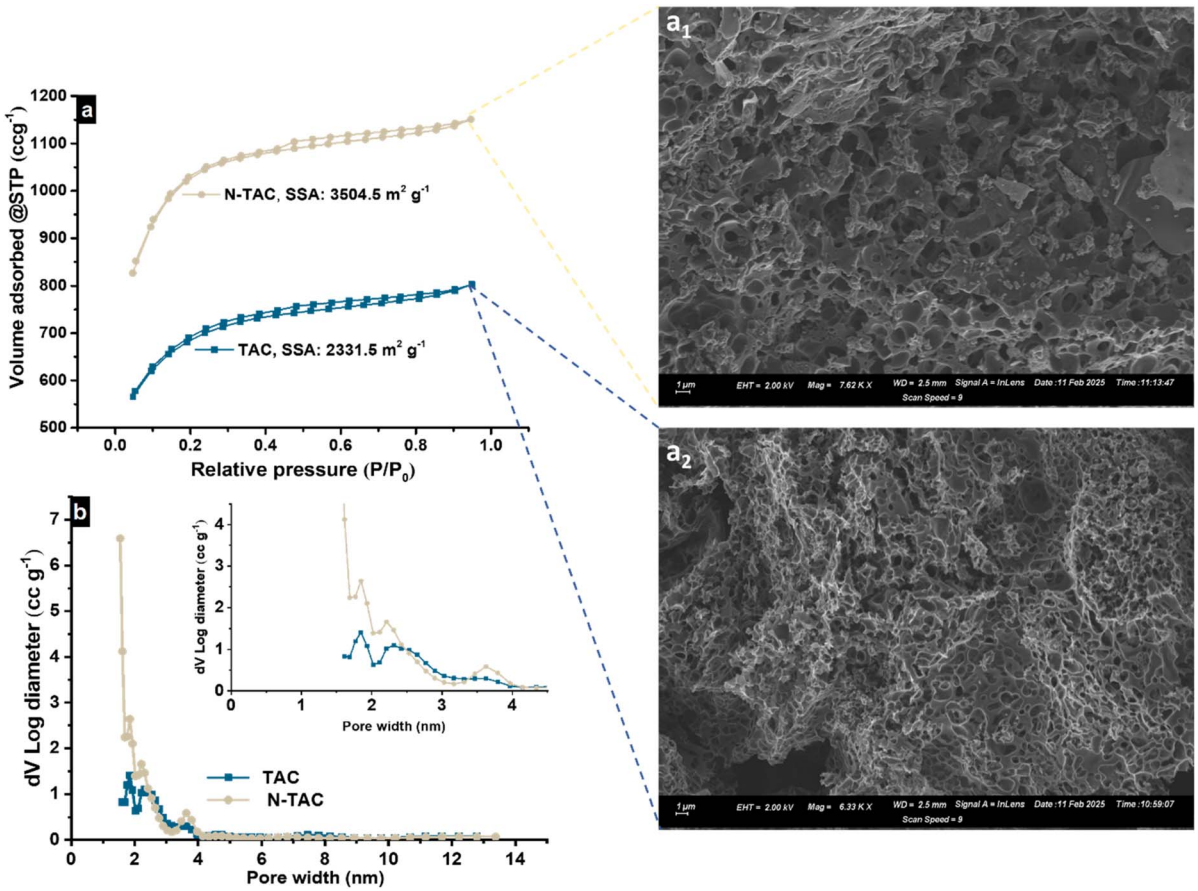

Fig. 1 Textural and morphological characterisation of TAC and N-TAC derived from Tondolo peels *via* K_2CO_3 activation at 700 °C. (a) Nitrogen adsorption–desorption isotherms showing Type IVa behavior with H4 hysteresis loops; (b) pore size distribution confirming micro-mesoporous architecture; (a_1) and (a_2) SEM micrographs of N-TAC and TAC respectively, illustrating the disordered interconnected microporous framework at low and high magnification.

Table 1 TAC and N-doped derivatives textural properties

Materials	TAC	N-TAC
Micropore volume (cc g^{-1})	0.86	1.38
Total pore volume (cc g^{-1})	1.61	1.61
Average pore size (nm)	2.14	2.04

carbon framework with interconnected microporous cavities in both samples, consistent with our previous findings.[1]

Table 2 presents a comparative analysis of various Nitrogen-sulfur co-doped activated carbons reported in the literature. While most of these materials exhibit respectable specific surface areas reaching 2000 m^2 g^{-1}, none approaches the exceptional value of 3504.5 m^2 g^{-1} achieved by our synthesized N-TAC. This remarkable surface area highlights the extraordinary textural properties obtained through the synergistic combination of Tondolo powder, K_2CO_3, and CH_4N_2O in the optimised 1 : 1 : 1 ratio. These results not only demonstrate superior performance metrics but also establish Tondolo as an outstanding precursor for the synthesis of highly porous carbon materials. The exceptional surface area of N-TAC directly contributes to its enhanced adsorption capabilities and electrochemical performance, positioning this material at the forefront of biomass-derived activated carbons for advanced applications.

3.2 Structural and chemical characterisation

Fig. 2 presents the Raman characterization of TAC (Fig. 2(a)) and N-TAC (Fig. 2(b)). While our previous work reported the basic Raman spectra, this study provides detailed Gaussian deconvolution to elucidate structural differences. Both samples exhibit the characteristic D (~1349.7 cm^{-1}) and G (~1600 cm^{-1}) bands of carbonaceous materials, with nearly identical I_D/I_G ratios (0.986 and 0.984, respectively). However, these simple ratios fail to capture the full structural complexity, necessitating deconvolution of the 1000–1800 cm^{-1} region. For TAC (Fig. 2(a)), the D_1, D_2, D_3, G, and D_4 components account for 51.36%, 22.27%, 13.97%, 12.12%, and 0.27% of the total area, confirming a highly defective framework with abundant edge sites generated during K_2CO_3 activation. N-TAC (Fig. 2(b)) exhibits markedly different fractions: 5.05% (D_1), 11.61% (D_2), 46.84% (D_3), 25.95% (G), and 10.55% (D_4). The reduced D_1 and enhanced G contributions indicate partial restoration of graphitic domains, while the dominant D_3 band reflects structural reorganization from nitrogen generation. The pronounced D_4 component confirms heteroatom C–N and C–O functionalities, consistent with successful nitrogen doping. The partial graphitization evidenced by the increased G band contribution in N-TAC is mechanistically significant: graphitic domains enhance in-plane electron delocalization, directly improving the electrical conductivity of the carbon framework and reducing charge transfer resistance at the electrode–electrolyte interface.[50] This structural ordering, driven by nitrogen-induced reorganization of the carbon lattice, complements the pseudocapacitive redox activity of pyridinic and pyrrolic nitrogen sites to collectively enhance electrochemical performance beyond what surface area alone could achieve.[51]

The Gaussian fitting achieved R^2 of 0.958 for TAC and 0.92 for N-TAC (Table 3), with modest fit quality reflecting genuine spectral complexity from overlapping bands. Overall, nitrogen doping reorganizes the carbon framework by reducing edge disorder, partially restoring graphitic order, and introducing surface functionalities, collectively explaining the improved electrochemical performance and selectivity of N-TAC.

X-ray Photoelectron Spectroscopy (XPS), previously reported in our earlier work, confirmed the surface chemistry and elemental composition of TAC and N-TAC (Fig. 3). Survey scans (Fig. 3(a)) revealed C 1s, O 1s, and O 2s peaks for both samples, with N-TAC displaying an additional N 1s peak, confirming nitrogen generated at the near-surface level of the AC (2.75 at%). High-resolution deconvolution (Fig. 3(b–c2)) identified sp^2 and sp^3 carbon configurations, oxygen functionalities (C–O, C=O, O–C=O), and four nitrogen species in N-TAC: pyridinic (42.3%, 398.1 eV), pyrrolic (31.5%, 400 eV), graphitic (20.1%, 401.7 eV), and oxidized forms (6%, 404.5 eV), which collectively enhance charge storage, conductivity, and adsorptive capacity. The dominance of pyridinic (42.3%) and pyrrolic (31.5%) nitrogen is particularly significant. Pyridinic nitrogen creates Lewis basic sites at edges that facilitate pseudocapacitive redox reactions

Table 2 Highly porous plant-based derived activated carbon

Precursor	Nitrogen source/ Dopant	Pre-treatment	Synthesis strategy	Specific surface area (m^2 g^{-1})	Ref.
Octadecyltrichlorosilane	$NaNH_2$	Yes	Low-temperature activation	2965	40
Chitosan	Self-doped	No	One-step preparation	2952	41
EDTA	Self-doped	No	Single-step scalable method	413	42
Bamboo	NH_3	Yes	Two-step method	2417	43
EDTA	Self-doped	No	One-step activation	2057	44
Pine sawdust	NH_3	No	One-step fabrication	1411	45
Polypyrrole (PPy)	Self-doped	No	One-pot synthesis	2160	46
Corncob	NH_3	No	One-step synthesis	1154	47
Rice husk	Chitosan	Yes	Two-step process	1496	48
Arundo donax	Self-doped	No	One-pot synthesis	982	49
Tondolo peels	Thiourea	No	Single pyrolysis-step co-doped carbonization/activation	3505	—

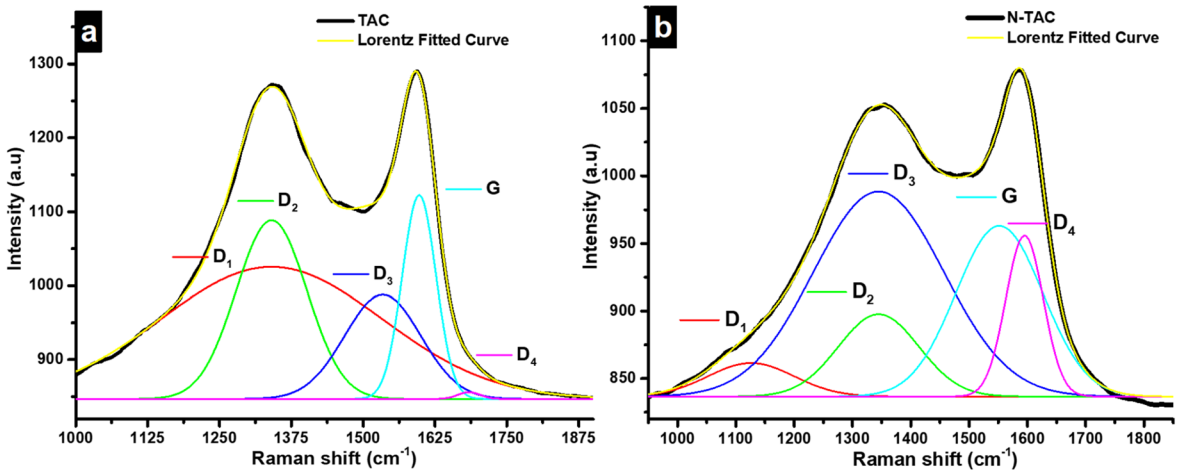

Fig. 2 Spectroscopic characterisation of TAC and N-TAC. (a and b) Raman spectra with five-component Gaussian deconvolution (D_1, D_2, D_3, G, D_4 bands) for TAC and N-TAC respectively, confirming partial graphitization and successful nitrogen incorporation in N-TAC. Deconvolution was performed over the 1000–1875 cm^{-1} range following the protocol of Sadezky *et al.*[52] and FWHM values bounded to physically meaningful limits. Goodness of fit was evaluated *via* R^2 and residual analysis ($R^2 > 0.90$ for all fits).

and electrostatic attraction of cationic pollutants, while pyrrolic nitrogen enhances surface wettability through hydrogen bonding with aqueous electrolytes, improving micropore ion accessibility.[53] Graphitic nitrogen raises the Fermi level to enhance electrical conductivity, and oxidized nitrogen provides additional polar sites for electrolyte affinity.[54] The synergistic interplay of these four configurations collectively accounts for the superior electrochemical and adsorptive performance of N-TAC over TAC.

The textural, morphological, and chemical characterization results confirm the successful synthesis of highly porous nitrogen-doped activated carbons from Tondolo peels. The carbon recovery analysis demonstrates the suitability of Tondolo peels as a biomass precursor, yielding 16% and 22% carbon recovery for TAC and N-TAC, respectively, comparable to conventional precursors such as coconut shells, peanut shells, and banana peels. This performance stems from the structural advantages of Tondolo peels, including inherent porosity and higher nitrogen content, which directly contribute to enhanced electrochemical and adsorptive capacity. Additionally, the regional availability of Tondolo fruit in tropical regions presents significant waste management benefits, converting agricultural waste into valuable functional materials and positioning Tondolo peels as a sustainable and economically viable alternative to conventional biomass precursors.

The potential reaction mechanisms underlying porous structure formation and nitrogen doping are illustrated in Fig. 4. The synthesis parameters were selected based on previous optimization studies, where 700 °C activation temperature and K_2CO_3 at a 1 : 1 precursor-to-activating agent ratio yielded optimal surface area development and structural integrity. During thermal treatment, K_2CO_3 engages in redox interactions with the carbon matrix, forming K–O–C intermediates and promoting CO/CO_2 evolution through carbon gasification, which creates the hierarchical porous network. For nitrogen-doped derivatives, CH_4N_2O (urea) thermally decomposes to serve as the nitrogen source, generating nitrogen within the developing porous carbon structure. Urea was selected over alternatives such as melamine and dicyandiamide due to its superior near-surface N functionalities generation on carbon. The thermal decomposition of urea proceeds through isocyanic acid (HNCO) and ammonia (NH_3) intermediates that

Table 3 Gaussian deconvolution parameters of Raman spectra for TAC and N-TAC

Sample	Peak	Position (cm^{-1})	Width (cm^{-1})	Area	Area (%)	Assignment
TAC	D_1	1340.5	384.6	86 183.7	51.36	Disordered graphitic lattice (A_1g)
	D_2	1340.5	123.3	37 367.5	22.27	Surface graphene layer (E_2g)
	D_3	1533.9	132.6	23 447.2	13.97	Amorphous carbon
	G	1597.3	58.8	20 344.2	12.12	Graphitic domains (E_2g)
	D_4	1684.2	38.8	448.6	0.27	C–O/C=O vibrations
					$R^2 = 0.958$	$\chi^2 = 446.6$
N-TAC	D_1	1126.1	147.6	4596.9	5.05	Disordered graphitic lattice (A_1g)
	D_2	1344.8	138.2	10 574.4	11.61	Surface graphene layer (E_2g)
	D_3	1344.8	224.1	42 671.1	46.84	Amorphous carbon
	G	1551.9	149.1	23 640.1	25.95	Graphitic domains (E_2g)
	D_4	1595.0	64.3	9613.1	10.55	C–N/C–O vibrations
					$R^2 = 0.920$	$\chi^2 = 287.9$

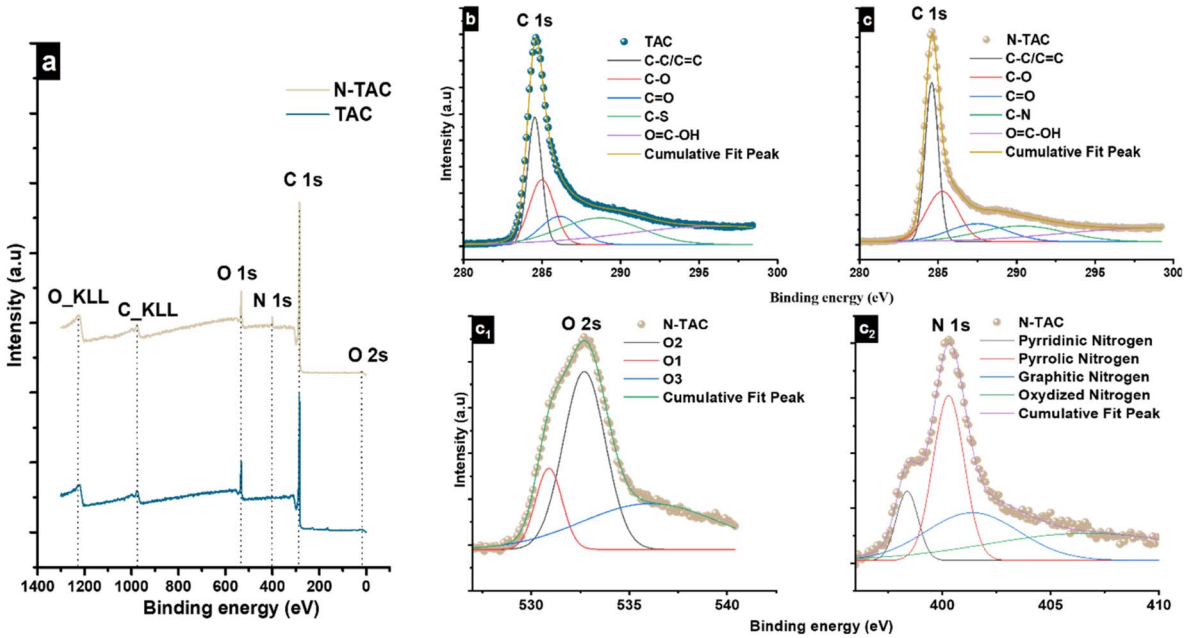

Fig. 3 XPS characterisation of TAC and N-TAC surface chemistry. (a) Survey spectra confirming C, O, and N elemental composition, with the N 1s peak exclusive to N-TAC (2.75 at%); (b) high-resolution C 1s spectrum of TAC; (c) high-resolution C 1s spectrum of N-TAC showing sp^2 and sp^3 carbon configurations; (c_1) O 1s spectrum of N-TAC identifying C–O, *C*=O, and O–C=O functionalities; (c_2) N 1s spectrum of N-TAC deconvoluted into pyridinic (42.3%, 398.1 eV), pyrrolic (31.5%, 400 eV), graphitic (20.1%, 401.7 eV), and oxidized nitrogen (6%, 404.5 eV) configurations. All spectra were fitted using pure Gaussian lineshapes on a Shirley background in OriginPro, with peak positions constrained to established literature ranges and FWHM values bounded to physically meaningful limits.

react with the carbon framework to form the pyridinic, pyrrolic, graphitic, and oxidized nitrogen configurations confirmed by XPS. The simultaneous presence of K_2CO_3 and urea decomposition products creates a synergistic etching and doping environment where K_2CO_3 drives porosity development while nitrogen incorporation stabilizes the pore structure and modifies surface chemistry, yielding a hierarchically porous nitrogen-rich carbon in a single pyrolysis step. Both porosity characteristics and heteroatom distribution are significantly influenced by dopant concentration. Compared to conventional multi-step approaches, this method integrates biochar formation, carbonization, and nitrogen doping into a single pyrolysis process, yielding hierarchical porous carbons with enhanced surface chemistry and higher porosity.

3.3 Three-electrode electrochemical analysis

Building upon the electrochemical comparison between TAC and N-TAC reported in our previously published work (Fig. S.1),[1,3] the CV curves (Fig. S.1a and b) recorded in both positive and negative potential windows revealed a clear distinction between the two materials. TAC exhibited rectangular profiles characteristic of pure electric double-layer capacitance (EDLC), while N-TAC displayed quasi-rectangular curves indicative of a hybrid EDLC/pseudocapacitive mechanism arising from nitrogen-induced faradaic active sites. N-TAC also extended the positive potential window to 0.8 V compared to 0.6 V for TAC, attributed to nitrogen functionalities stabilising the carbon framework against oxidation, while its negative potential window was slightly reduced to −0.8 V relative to −0.9 V for TAC, associated with nitrogen functional groups promoting hydrogen evolution at negative potentials. GCD profiles (Fig. S.1(c) and (d)) further supported these findings, with N-TAC displaying longer charge–discharge times and highly symmetric triangular curves, confirming enhanced specific capacitance, superior electrochemical reversibility, and improved electronic conductivity from graphitic nitrogen doping. Collectively, these results establish N-TAC as the superior electrode material, providing the basis for the detailed characterisation presented in Fig. 5. CV curves in positive (Fig. 5(a)) and negative (Fig. 5(b)) potential windows reveal quasi-rectangular shapes with slight distortions, indicating the coexistence of EDLC and pseudocapacitive charge storage mechanisms. The negative potential CVs exhibit higher current response than the positive window (at identical scan rates), attributed to the asymmetric distribution of charge storage mechanisms with the negative electrode benefiting from enhanced cation (Na^+) adsorption into the nitrogen-rich microporous structure, while nitrogen functionalities (particularly pyridinic and pyrrolic) undergo more favourable redox reactions under cathodic polarization, providing additional pseudocapacitive contribution. Notably, at lower scan rates (*e.g.*, 5 mV s^{-1}), the CV profiles exhibit slight distortions due to the slower faradaic contributions becoming more pronounced, while higher scan rates (*e.g.*, 20 mV s^{-1}) suppress these slower redox processes, yielding more rectangular profiles dominated by double-layer capacitance.[10] The nitrogen functionalities characterized in Fig. 3(c_2) introduce redox-active sites that facilitate faradaic reactions. Pyridinic nitrogen provides lone

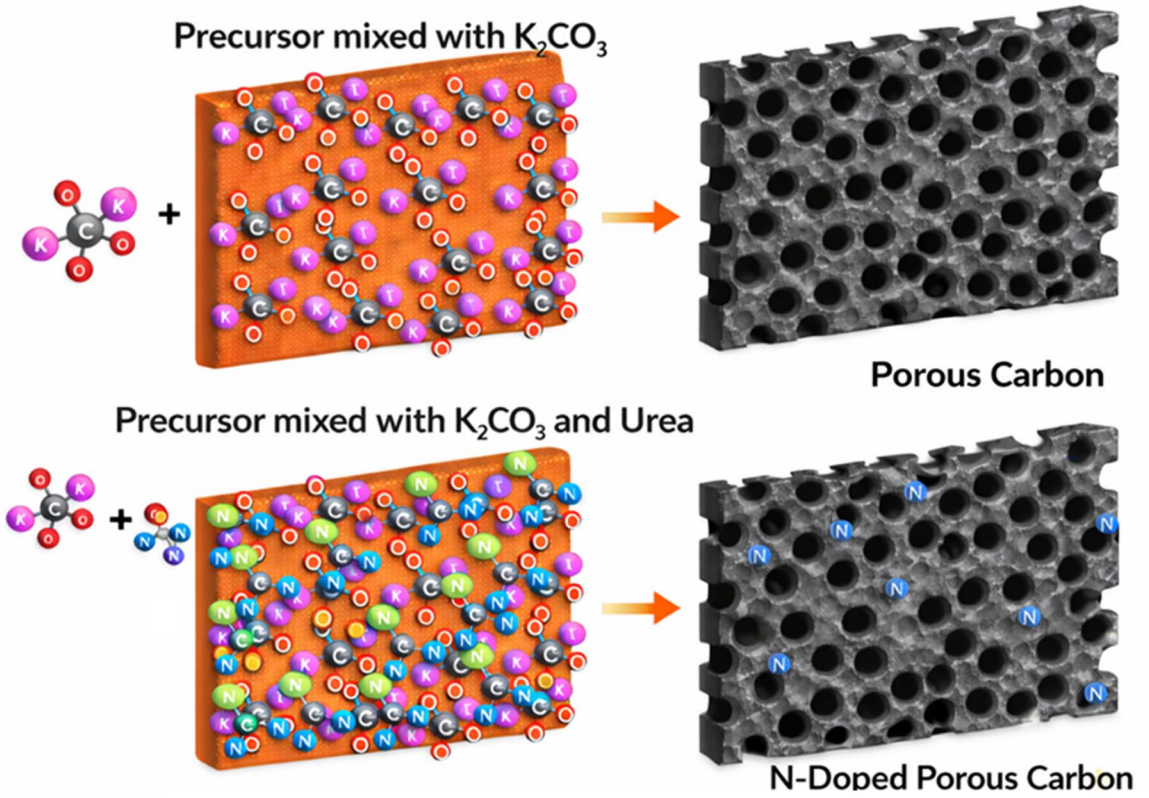

Fig. 4 Schematic reaction mechanism for the single pyrolysis synthesis of TAC and N-TAC from Tondolo peels, illustrating K_2CO_3-driven carbon gasification and pore formation through K–O–C intermediate generation, and urea thermal decomposition producing NH_3 and HNCO intermediates that incorporate pyridinic, pyrrolic, graphitic, and oxidized nitrogen functionalities into the developing carbon framework at 700 °C.

pair electrons that create Lewis basic sites for redox reactions. In contrast, pyrrolic nitrogen enhances surface wettability through hydrogen bonding with the aqueous electrolyte, improving ion accessibility and micropore penetration. Oxidized nitrogen species, though present in smaller quantities, provide additional polar sites that enhance electrolyte wettability through dipole–dipole interactions. In the negative potential region (Fig. 5(b)), N-TAC maintains capacitive behavior within an optimized −0.8 V window to prevent hydrogen evolution.

Fig. 5(c) presents the EIS Nyquist plot with fitted data and equivalent circuit (inset). N-TAC demonstrates a low equivalent series resistance (ESR) of 2.05 Ω in 1 M $NaNO_3$ electrolyte, indicating excellent electrical conductivity. $NaNO_3$ was selected as the electrolyte due to its superior ionic conductivity compared to Na_2SO_4, wider electrochemical stability window than KOH (which suffers from oxygen evolution at positive potentials), and lower cost and environmental safety compared to organic electrolytes. Additionally, the relatively small ionic radius of Na^+ facilitates favorable intercalation kinetics within the microporous carbon framework. The Nyquist plot exhibits a soft semicircle in the high-frequency region, confirming minimal charge transfer resistance at the electrode–electrolyte interface. Nonlinear least-squares fitting (Z-fit) using the equivalent circuit model (inset) yielded $R = 2.05$ Ω (solution resistance), matching the ESR value, and $R_{CT} = 2.75$ Ω (charge transfer resistance). The model incorporates constant phase elements (Q_2, Q_3) rather than ideal capacitors to account for surface heterogeneity and non-ideal capacitive behaviour. This low charge-transfer resistance correlates with N-TAC's high specific surface area and substantial micropore volume, which enable efficient interaction of Na^+ and NO_3^- ions with the microporous structure. Additionally, nitrogen functionalities create electron-rich regions within the carbon framework, thereby facilitating faster electron-transfer kinetics. The near-vertical line in the low-frequency region indicates pseudocapacitive behaviour with efficient ion diffusion. These EIS results confirm that nitrogen doping effectively reduces both electronic and ionic transport resistances, thereby enhancing the overall electrochemical performance of N-TAC.

Fig. 5(d) presents the frequency-dependent real (C') and imaginary (C'') capacitance, providing insight into the electrode's relaxation dynamics. The real capacitance reaches 0.12 F at low frequencies, representing the total charge storage capacity accessible during slow charge–discharge processes. The imaginary capacitance exhibits a maximum of 0.29 F, corresponding to energy dissipation due to resistive and dielectric losses during ion transport. The relaxation time constant (τ = 0.87 s), derived from the frequency at maximum imaginary capacitance, indicates relatively fast ion diffusion kinetics

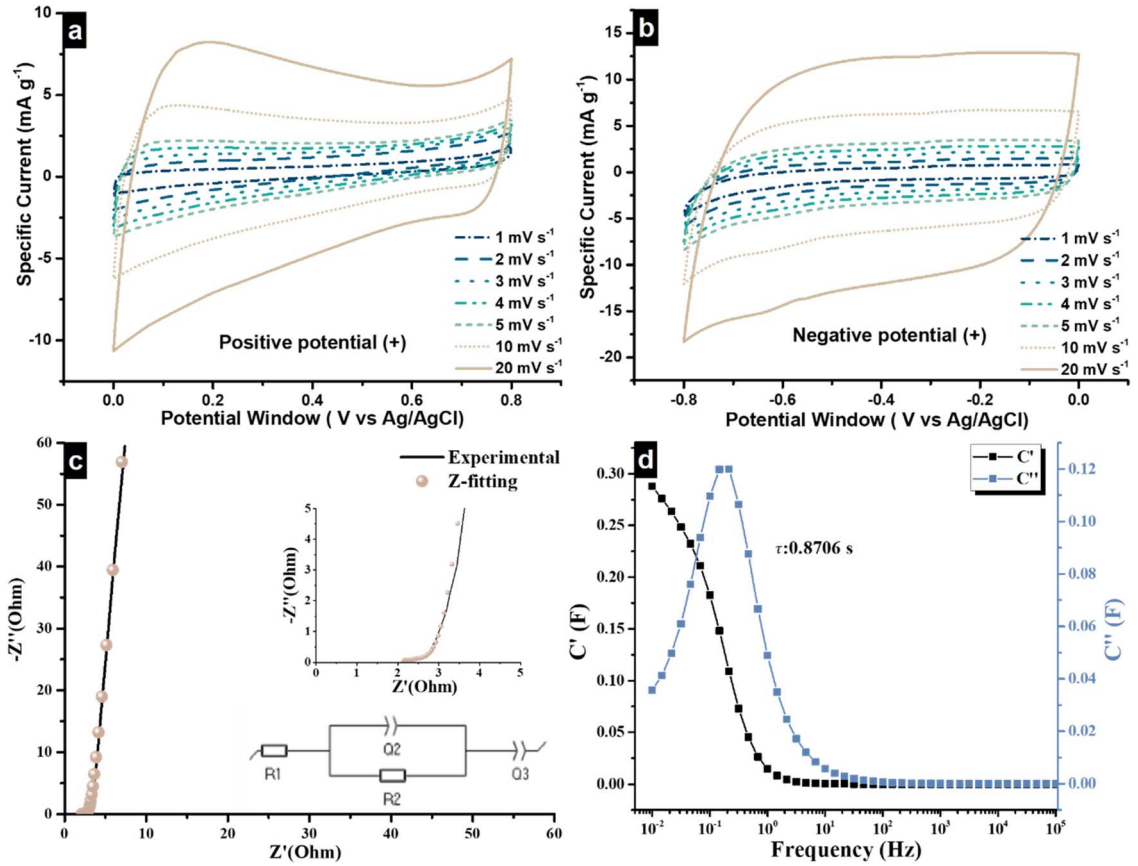

Fig. 5 Three-electrode electrochemical characterisation of N-TAC in 1 M $NaNO_3$ electrolyte. CV profiles in the (a) positive (0 to +0.8 V) and (b) negative (0 to −0.8 V) potential windows at scan rates of 1–20 mV s^{-1}, showing quasi-rectangular profiles indicative of coexisting EDLC and pseudocapacitive charge storage; (c) EIS Nyquist plot with nonlinear least-squares fit and equivalent circuit model (inset), yielding ESR = 2.05 Ω and R_{CT} = 2.75 Ω; (d) frequency-dependent real (C') and imaginary (C'') capacitance plots with relaxation time constant τ = 0.87 s determined from the frequency at maximum C''.

within the N-TAC microporous network. This rapid response time is attributed to the hierarchical pore structure and enhanced electrolyte wettability from nitrogen functionalities, enabling efficient charge storage even at moderate frequencies. The EIS analysis confirms that nitrogen doping effectively reduces both electronic and ionic transport resistances, thereby enhancing the electrochemical performance of N-TAC.

3.3.1 Charge storage mechanism analysis. To quantitatively delineate the charge storage mechanisms of N-TAC, power law analysis was conducted across scan rates of 1–20 mV s^{-1} in both potential windows using the relationship $i = av^b$ and eqn (S.2) (SI), where b-values approaching 1.0 and 0.5 indicate surface-controlled (EDLC) and diffusion-controlled (battery-type) processes, respectively (Fig. S.2(a and b)).[55] In the positive window, the extracted b-values decrease systematically from 0.981 at 0.1 V to 0.500 at 0.7 V (Fig. 6(a)), reflecting a progressive transition from double-layer charging at low potentials toward diffusion-controlled faradaic behavior at higher potentials, where nitrogen redox functionalities become increasingly active under anodic polarization. This evolution is mechanistically rooted in the potential-dependent activity of pyridinic and pyrrolic nitrogen sites: at low anodic potentials these sites engage in kinetically fast proton-coupled electron transfer, yielding b near unity, whereas progressive oxidation at higher potentials shifts charge storage toward ion-diffusion-limited faradaic processes confined within the micropore network, driving b toward 0.50. In the negative window (Fig. 6(b)), b-values of 0.840, 0.908, and 0.821 at −0.3, −0.5, and −0.7 V confirm predominantly surface-controlled behavior under cathodic polarization, driven by rapid Na^+ adsorption and pseudocapacitive redox activity of pyridinic and pyrrolic nitrogen functionalities. The sustained high b-values reflect the electrochemical inactivity of nitrogen redox sites under cathodic polarisation, where double-layer formation dominates and the kinetic constraints imposed by faradaic nitrogen reactions are absent, mechanistically accounting for the asymmetry between the two potential windows. The modest b-value of 0.631 at −0.1 V suggests a minor diffusive contribution near the open-circuit potential that diminishes with increasing cathodic polarization. All fits yielded $R^2 > 0.983$, confirming the robustness of the power law model. To further quantify these contributions, Trasatti deconvolution was performed using eqn (S.3)–(S.7). The capacitive and pseudocapacitive contributions were determined by extrapolating C_s^{-1} *versus* $v^{1/2}$ as $v \to \infty$ and

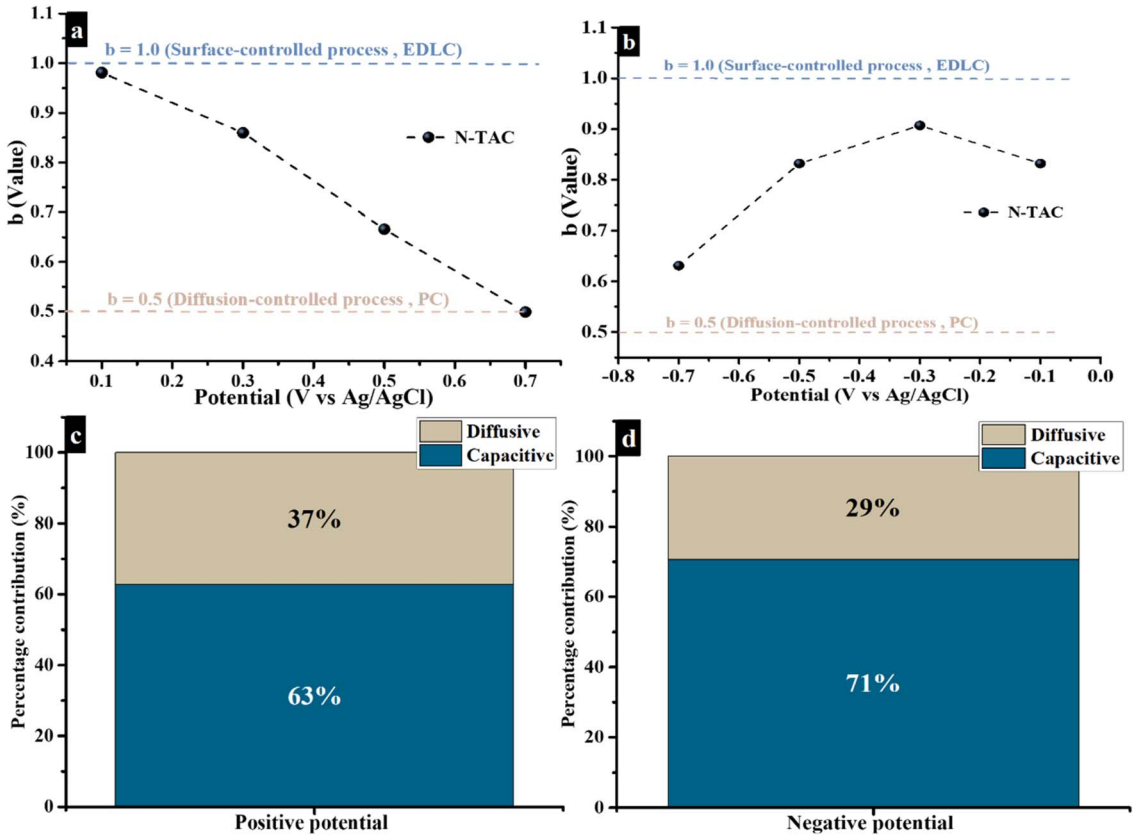

Fig. 6 Power law and Trasatti analysis of N-TAC in 1 M $NaNO_3$. (a and b) *b*-values derived from the power law relationship $i = av^b$ as a function of applied potential for the positive (0.1–0.7 V) and negative (−0.1 to −0.7 V) windows respectively, where $b = 1.0$ indicates surface-controlled (EDLC) and $b = 0.5$ indicates diffusion-controlled (PC) charge storage. (c and d) Histograms of capacitive (EDLC) and diffusion-controlled (PC) charge contributions determined by Trasatti deconvolution for the positive (EDLC: 63%; PC: 37%) and negative (EDLC: 71%; PC: 29%) windows respectively.

C_s *versus* $v^{-1/2}$ as $v \rightarrow 0$, yielding q_{outer} and q_{total}, respectively (Fig. S.3). In the positive window, capacitance decreases from 312.8 to 160.1 F g^{-1} with increasing scan rate, with the outer capacitance accounting for 63% of total charge and 37% diffusion-controlled (Fig. 6(c)). In the negative window, substantially higher capacitance values of 541.4–313.6 F g^{-1} confirm enhanced charge storage under cathodic polarization, with the outer contribution rising to 71% and the diffusive fraction reduced to 29% (Fig. 6(d)). These findings are mutually consistent: The greater diffusive fraction in the positive window aligns with *b*-values declining toward 0.5 at higher potentials, while the dominant capacitive fraction in the negative window corroborates the surface-controlled behavior indicated by *b*-values above 0.8, collectively confirming the asymmetric but surface-dominated charge storage nature of N-TAC.

To complement the Trasatti deconvolution, Dunn's method was applied using $i(V) = k_1v + k_2v^{1/2}$, with k_1 and k_2 extracted from $iv^{1/2}$ *versus* $v^{1/2}$ plots at several potential windows (Fig. S.4). In the positive window (Fig. 7(a)), the capacitive contribution varies non-monotonically between 27.9% and 64.1% across 1–5 mV s^{-1}, reflecting the complex interplay between nitrogen redox functionalities and double-layer charging under anodic polarization.[55] In the negative window (Fig. 7(b)), a clear monotonic increase from 35.0% to 54.6% confirms progressive dominance of surface-controlled mechanisms with increasing scan rate. At 20 mV s^{-1}, CV current separation (Fig. 7(c and d)) reveals EDLC contributions of 70.5% and 70.6% in the positive and negative windows respectively, confirming overwhelmingly surface-controlled charge storage at fast scan rates, consistent with the power law and Trasatti analyses.

3.3.2 Symmetric device performance. To validate the practical application potential of the optimized N-TAC material, a symmetric supercapacitor device (N-TAC//N-TAC) was fabricated with 1 M $NaNO_3$ as the electrolyte. The device was assembled with electrodes mass-balanced according to eqn (3), establishing a negative-to-positive electrode mass ratio of approximately 1.2, with a total electrode mass loading of 5.0 mg cm^{-2}. Fig. 8(a) demonstrates the device's CV characteristics across various scan rates within an operational voltage window of 1.7 V. Although the individual three-electrode potential windows of the positive (0 to +0.8 V) and negative (0 to −0.8 V) electrodes sum to 1.6 V, the device voltage was experimentally extended to 1.7 V through careful optimization, enabled by the electrochemical stability of N-TAC and the wide stability window of 1 M $NaNO_3$, without compromising capacitive behaviour or inducing parasitic decomposition reactions. The

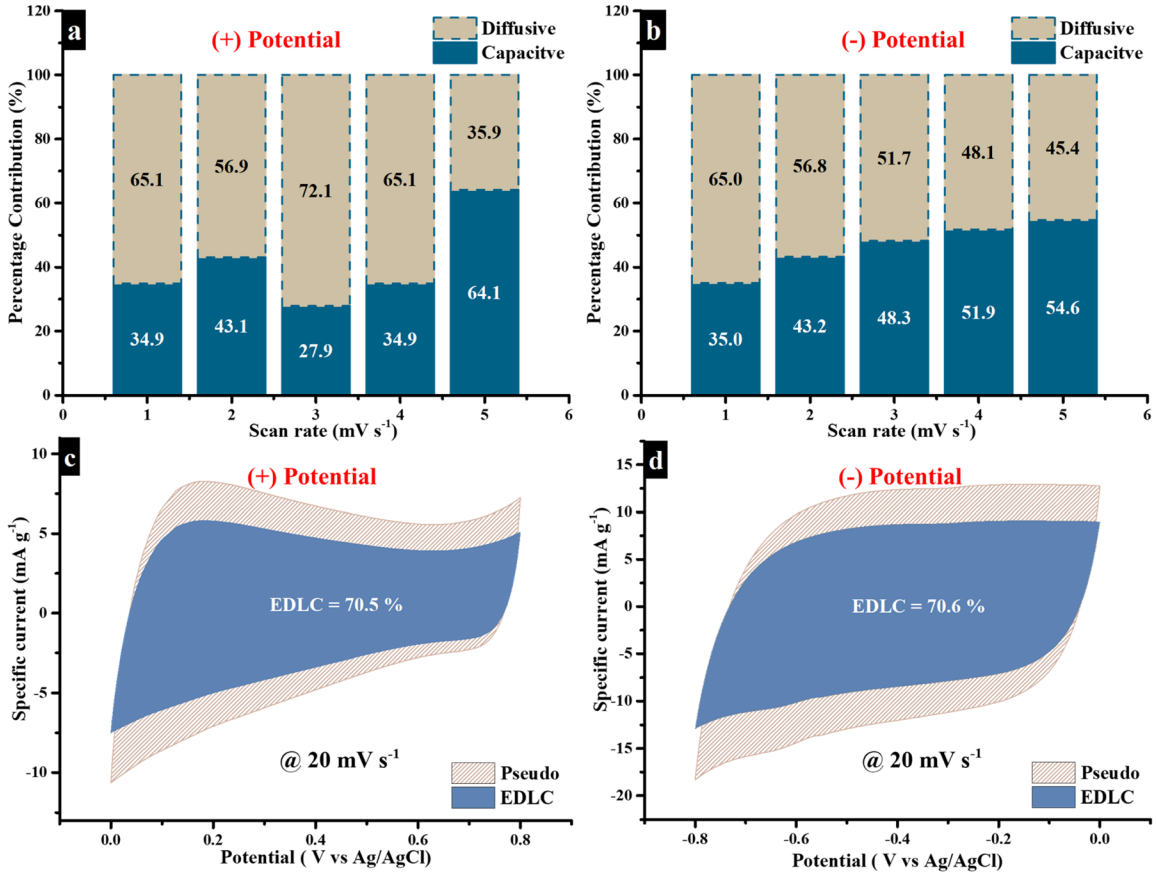

Fig. 7 Dunn's method charge storage analysis of N-TAC in 1 M $NaNO_3$, separating capacitive (EDLC) and diffusion-controlled (PC) current contributions using $i(V) = k_1v + k_2v^{0.5}$. (a and b) Histograms of EDLC and PC percentage contributions at scan rates of 1–5 mV s^{-1} for the positive and negative potential windows respectively. (c and d) CV current separation plots at 20 mV s^{-1} showing the surface-controlled (shaded) and diffusion-controlled contributions for the positive (EDLC = 70.5%) and negative (EDLC = 70.6%) windows respectively.

device maintains quasi-rectangular CV profiles even at elevated scan rates, indicating excellent capacitive behaviour with pseudocapacitive contributions.[56] This shape retention at higher scan rates confirms rapid charge–discharge capabilities and efficient electrolyte ion transport through the hierarchical porous structure of N-TAC. The GCD profiles presented in Fig. 8(b) exhibit semi-triangular/semi-linear characteristics at different specific currents, further validating the pseudocapacitive charge storage mechanism.[57] The slight deviation from perfectly triangular shapes aligns with the nitrogen-induced faradaic contributions identified in three-electrode measurements.

As shown in Fig. 8(c), the device delivers a remarkable single-electrode specific capacitance of 118.2 F g^{-1} at 0.5 A g^{-1}, maintaining substantial capacitance retention even at a high current density of 10 A g^{-1}. This rate capability demonstrates the effectiveness of nitrogen doping in enhancing electronic conductivity and facilitating rapid ion diffusion. The cycling stability evaluation (Fig. 8(d)) conducted at 5 A g^{-1} reveals great performance with the device maintaining 94% of its initial capacitance after 10 000 charge–discharge cycles. This high retention confirms the structural robustness of N-TAC electrodes and stability of nitrogen functionalities under repeated cycling. Moreover, the coulombic efficiency exceeds 100% throughout the cycling process, suggesting gradual electrode activation phenomena.[9,58] This indicates gradual electrode activation through progressive electrolyte wetting of initially inaccessible micropores and electrochemical activation of nitrogen sites under repeated polarization. The minor 6% capacitance fade is attributed to inevitable binder and partial nitrogen functionality degradation. This represents an improvement over our previously reported coulombic efficiency due to optimized electrode fabrication, including better binder distribution and enhanced electrode-current collector contact. The relatively low initial coulombic efficiency is attributed to irreversible processes including incomplete electrolyte wetting of deeply buried micropores, interfacial passivation layer formation, and occupation of high-energy nitrogen-functional sites during initial ion adsorption. As cycling progresses, the coulombic efficiency rapidly stabilizes and consistently exceeds 100%, reflecting gradual electrode activation through progressive micropore wetting and electrochemical activation of nitrogen redox sites. This well-documented behavior in nitrogen-doped porous carbons arises from faradaic contributions of nitrogen functionalities during discharge, yielding

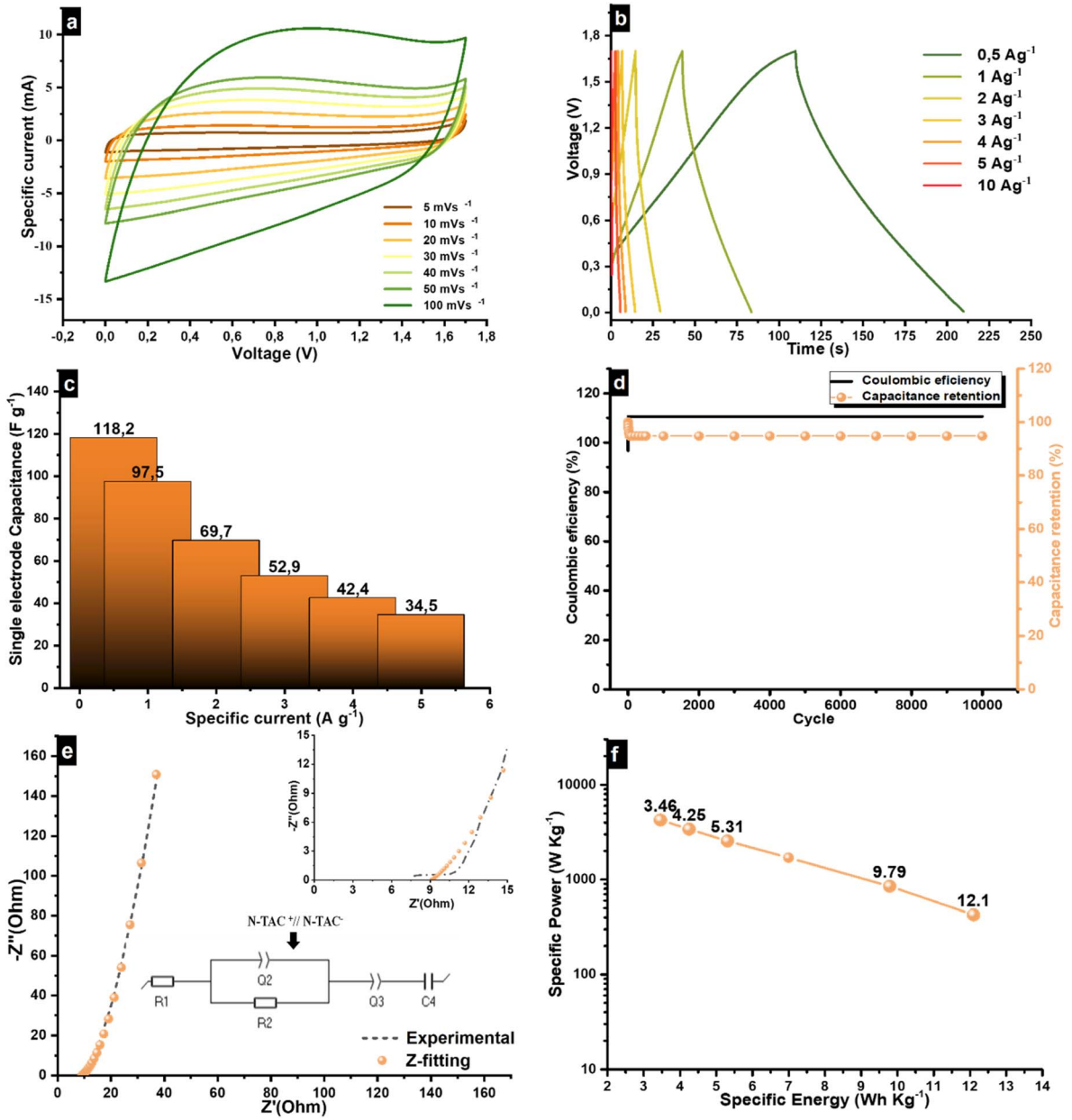

Fig. 8 Electrochemical performance of the symmetric N-TAC//N-TAC supercapacitor device in 1 M $NaNO_3$ electrolyte within a 1.7 V operating window. (a) CV profiles at scan rates of 5–100 mV s^{-1}; (b) GCD curves at current densities of 0.5–10 A g^{-1}; (c) specific capacitance as a function of current density; (d) cycling stability showing 94% capacitance retention after 10 000 charge–discharge cycles at 5 A g^{-1}; (e) EIS Nyquist plot before and after cycling; (f) Ragone plot comparing energy and power density of N-TAC//N-TAC with literature-reported symmetric carbon-based devices.

discharge capacities marginally exceeding charge capacities during the initial activation period.[1]

The electrochemical impedance spectroscopy results (Fig. 8(e)) indicate an ESR of approximately 7 Ω with negligible semicircle formation in the high-frequency region, confirming minimal charge transfer resistance (R_{CT}: 9.5 Ω) at the electrode–electrolyte interface. The equivalent circuit model derived from nonlinear least square fitting comprises resistors (R_1 (solution resistance), R_2 (charge transfer resistance)), constant phase elements (Q_2, Q_3) associated with mass transfer processes, and a capacitor (C_4) confirming the device's capacitive nature.[59,60] The Ragone plot (Fig. 9(f)) positions the N-TAC//N-TAC device favourably among comparable supercapacitor systems, demonstrating competitive or superior specific energy (12.1 Wh Kg^{-1}) and specific power (425 WKg^{-1}) at 0.5 A g^{-1} as compared to previously reported biomass-derived carbon-based devices (Table 4). This performance in a practical device configuration underscores the significant potential of nitrogen-doped Tondolo shell-derived activated carbon for sustainable energy storage applications. The exceptional electrochemical performance of the symmetric device can be attributed to the synergistic effects of optimized nitrogen content, hierarchical

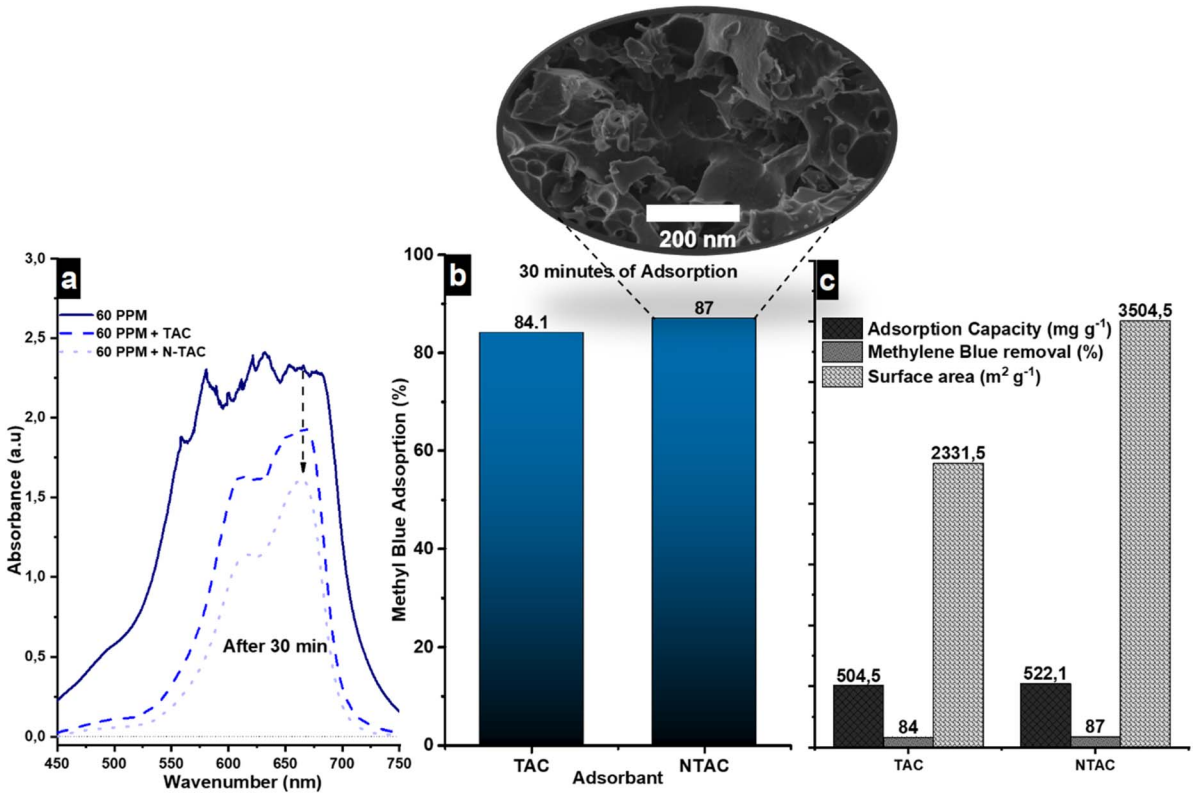

Fig. 9 Methylene blue adsorption comparison of TAC and N-TAC at 50 ppm initial concentration with 10 mg adsorbent in 50 mL solution. (a) UV-visible absorption spectra at 665 nm as a function of contact time; (b) adsorption efficiency (%) *versus* contact time; (c) comparison of equilibrium removal percentages and adsorption capacities (mg g^{-1}) for TAC and N-TAC, demonstrating the superior performance of N-TAC attributed to nitrogen-enhanced surface chemistry.

porosity, and enhanced surface functionality in the N-TAC material. These properties collectively facilitate rapid charge transfer, efficient ion transport, and stable electrode–electrolyte interfaces, essential requirements for high-performance supercapacitor applications.

Post-cycling EIS analysis (Fig. S.5(a)) reveals increased charge transfer resistance, indicating electrode–electrolyte interface deterioration from continuous ion adsorption/desorption and potential side reactions. Post-cycling SEM (Fig. S.5(b)) shows partial pore blockage from binder degradation, restricting ion transport and reducing accessible surface area. Future improvements include binder-free electrode fabrication to eliminate pore blockage and extend the stable voltage window, alongside electrolyte modification using organic or ionic liquid electrolytes to minimize decomposition reactions and enhance long-term cycling stability.

3.4 Methylene blue adsorption performance

Fig. 9 presents a comparative assessment of the adsorption capabilities of TAC and N-TAC using methylene blue (MB) as a model cationic pollutant at a concentration of 60 ppm over 30

Table 4 Electrochemical performance comparison of N-TAC symmetric supercapacitor with similar carbon-based devices

Precursor source (N-Doped AC)	Electrolyte	Specific capacitance (F g^{-1})	Energy density (Wh kg^{-1})	Power density (W kg^{-1})	Ref.
Coal	6 M KOH	287 @ 0.5 A g^{-1}	10.0	250	61
Raw leather trimming waste	1 M H_2SO_4	257 @ 0.5 A g^{-1}	6.95	9972	62
Pueraria	6 M KOH	250 @ 0.5 A g^{-1}	8.46	123	63
Boat-fruited sterculia seed	6 M KOH	72.3 @ 0.5 A g^{-1}	10.04	250	64
Camellia husk	6 M KOH	87.3 @ 0.5 A g^{-1}	12.11	250	65
Natural casings	6 M KOH	42.6 @ 0.5 A g^{-1}	11.6	297	66
Polyacrylonitrile	6 M KOH	51 @ 0.5 A g^{-1}	4.5	200	67
SiO_2-derived	6 M KOH	321 @ 0.5 A g^{-1}	11.2	125.1	68
Sawdust	6 M KOH	249 @ 0.5 A g^{-1}	8.7	251.6	69
Polyacrylamide/lignocellulose aerogel	6 M KOH	312 @ 0.5 A g^{-1}	11.8	230	70
Tondolo peels (this work)	1 M $NaNO_3$	118.2	12.1	425	—

minutes. All calculations were validated against the calibration curve at the Methylene Blue absorption maximum (665 nm) shown in Fig. S.6.

UV-visible spectroscopy results (Fig. 9(a)) demonstrate a faster decrease in MB's characteristic absorption peak for N-TAC compared to TAC, indicating accelerated adsorption kinetics in the nitrogen-doped material. Quantitative analysis of adsorption efficiency (Fig. 9(b)) reveals that N-TAC achieves a superior removal performance of 87% compared to TAC's 84% after 30 minutes of contact time. The inset SEM images demonstrate excellent structural stability, showing no significant morphological changes in the sample following the adsorption process. Fig. 9(c) presents a comparison of removal percentages and adsorption rates correlated with the respective surface areas of both materials. N-TAC demonstrates superior performance across all metrics, confirming the benefits of nitrogen doping on adsorption capabilities.[30] This enhanced performance can be attributed to synergistic mechanisms involving nitrogen functionalities creating localized negative charge centers within the carbon framework which promotes strong electrostatic interactions with cationic MB molecules.[30]

3.4.1 Adsorption kinetics. The effect of N-TAC mass loading on MB adsorption efficiency was conducted as illustrated in Fig. 10(a). The results demonstrate a direct correlation between adsorbent dosage and removal efficiency, with adsorption performance improving progressively as the mass loading increased. At the highest evaluated dosage of 30 mg, N-TAC achieved a great removal efficiency of 92.4% within just 5 minutes of contact time. This enhanced performance with increasing adsorbent mass can be attributed to the greater availability of active adsorption sites and the larger interfacial surface area accessible to MB molecules in solution.[71]

The adsorption kinetics of methylene blue onto nitrogen-doped activated carbon was investigated using pseudo-first order and pseudo-second-order kinetic models at three initial concentrations (20, 40, and 60 ppm) with a fixed adsorbent dosage of 10 mg in 50 mL solution volume (Fig. 10(b) and (c)). The time-dependent concentrations were determined from the characteristic MB absorption peaks in UV-visible spectra illustrated in Fig. S.7(a)–(c). These three concentration levels were deliberately selected to represent a range of dye loading conditions, allowing investigation of adsorption behavior from relatively dilute to moderately concentrated MB solutions, and to examine how the surface chemistry of N-TAC responds across different adsorbate-to-adsorbent ratios.

At the lowest concentration evaluated (20 ppm), MB molecules encounter an abundance of available active sites relative to the number of dye molecules in solution. Under these conditions, high-energy nitrogen-functionalized surface sites, including pyridinic and pyrrolic nitrogen groups, preferentially interact with MB through strong electrostatic attractions and chemisorptive bonding. The large excess of active sites relative to dye molecules at this concentration ensures rapid and highly efficient removal, as reflected in the UV-visible spectra in Fig. S.7(a), where the characteristic MB absorption peak diminishes sharply within the initial 20 minutes of contact. At this concentration range, the sensitivity of UV-visible measurements is particularly important, as small changes in absorbance must be reliably resolved to accurately track the adsorption process, analogous to working near the limit of quantification of the analytical system. From a diffusion perspective, at 20 ppm the low adsorbate concentration maintains a steep concentration gradient between the bulk solution and the pore interior, driving rapid intraparticle diffusion into the microporous network with minimal resistance, such that external film diffusion and surface adsorption remain the dominant rate-controlling steps.

As the initial concentration increases to 40 ppm, the ratio of MB molecules to available active sites shifts, and the adsorption

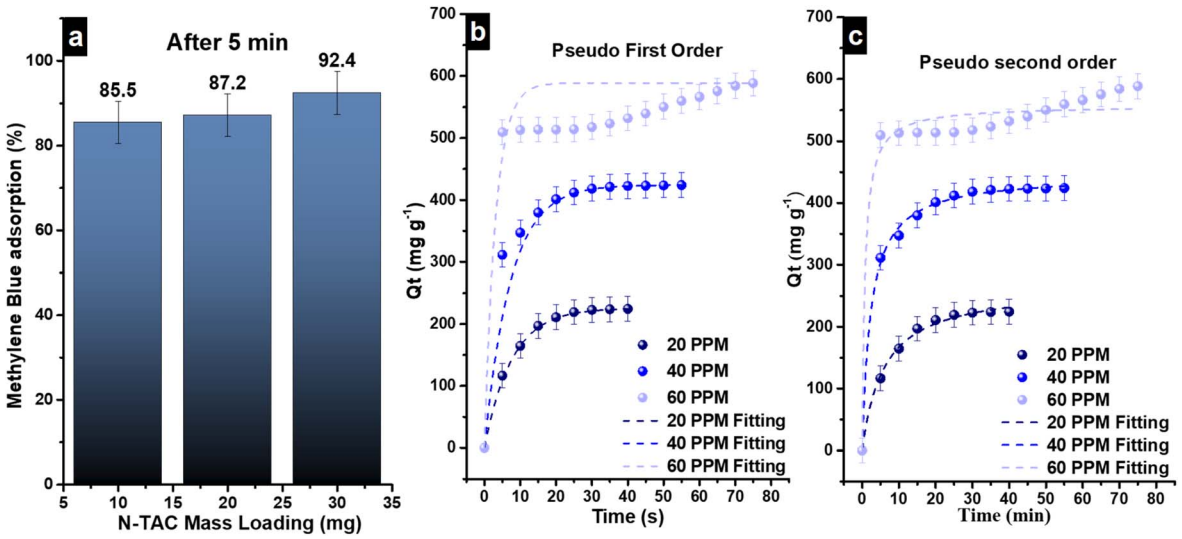

Fig. 10 N-TAC methylene blue adsorption evaluation. (a) Effect of adsorbent mass loading (5–30 mg) on MB removal efficiency (%) at 50 ppm with error bars representing standard deviation from triplicate measurements; (b) pseudo-first-order and (c) pseudo-second-order kinetic model fits for MB adsorption at initial concentrations of 20, 40, and 60 ppm with 10 mg N-TAC in 50 mL solution, showing superior fit of pseudo-second-order kinetics (R^2 = 0.99–0.97) and equilibrium adsorption capacities of 265.9–557.6 mg g^{-1}.

process becomes progressively governed by a broader distribution of surface sites. While high-energy sites continue to contribute, lower-energy sites begin to participate more significantly in the adsorption process. This transition is reflected in the UV-visible spectra of Fig. S.7(b), where the rate of peak attenuation is slightly slower compared to the 20 ppm case, indicating a more gradual approach to equilibrium as the surface becomes more heterogeneously engaged. At this intermediate concentration, intraparticle diffusion resistance within the micropores begins to play a more significant role, as the higher adsorbate flux toward the carbon surface progressively fills external and mesopore sites, forcing MB molecules to diffuse deeper into the microporous network where tortuous pore pathways and narrowing pore diameters impose increasing resistance to mass transfer.

At the highest concentration studied (60 ppm), the system operates under conditions where the adsorbate supply more closely approaches the capacity limits of the N-TAC surface. Lower-energy adsorption sites are now extensively involved, and the adsorption mechanism becomes more complex, involving not only chemisorption at nitrogen-functional sites but also contributions from physical adsorption within the developed pore network. At this concentration, intraparticle diffusion resistance becomes the dominant rate-limiting factor, as near-saturation of external and mesopore sites compels MB molecules to penetrate deeper into the micropore network (micropore volume 1.38 cc g^{-1}), where pore constriction, tortuosity, and competitive site occupation retard diffusion kinetics.

This progressive shift from surface-controlled to diffusion-limited adsorption with increasing concentration is mechanistically consistent with the pseudo-second-order model, which implicitly accounts for the heterogeneous chemisorptive interactions and diffusion limitations becoming increasingly prominent at higher dye loadings. This complexity is evidenced by the slower decay of the MB absorption peak in Fig. S.7(c) and is further reflected analytically in the decreasing R^2 values observed for both kinetic models at this concentration, indicating that neither a simple first- nor second-order model fully captures the heterogeneity of the adsorption process at higher dye loadings. From an analytical perspective, working at these higher concentration levels moves the system toward conditions where surface saturation, rather than measurement sensitivity, becomes the primary limiting factor governing removal efficiency.

While the pseudo-first-order model demonstrated good correlation with experimental data (R^2 = 0.99, 0.98, and 0.96), the pseudo-second-order model exhibited superior fit with consistently higher correlation coefficients (R^2 = 0.99, 0.99, and 0.97) and equilibrium adsorption capacities ranging from 265.9 to 557.6 mg g^{-1} as illustrated in Table 5. The excellent fit to pseudo-second-order kinetics indicates that the adsorption mechanism is predominantly governed by chemisorption involving valence forces through electron sharing or exchange between the adsorbent and adsorbate, suggesting strong interactions between methylene blue molecules and nitrogen-containing functional groups on the carbon surface. The increase in equilibrium adsorption capacities with initial concentration for both models demonstrate efficient utilization of heterogeneous binding sites, with high-energy sites occupied first at low concentrations followed by progressive occupation of lower-energy sites. The concentration-dependent transition from surface-controlled to diffusion-limited kinetics confirms the dual role of N-TAC's hierarchical pore structure: mesopores facilitate rapid MB transport toward adsorption sites, while micropores provide the high-density active site environment responsible for the exceptional adsorption capacity.

The remarkable adsorption performance can be attributed to the synergistic effects of high surface area, well-developed pore structure, and enhanced surface chemistry resulting from nitrogen generated on the carbon surface, which creates additional active sites and modifies the electronic properties of the carbon surface to promote stronger adsorbent–adsorbate interactions.[72] This finding aligns with the understanding of the nitrogen-doping effects, as the introduced nitrogen functionalities create specific binding sites that interact with MB molecules through electrostatic attractions. Furthermore, the decreasing trend in R^2 values with increasing initial MB concentration observed for both models indicates that the adsorption mechanism becomes more complex at higher concentrations. Among the nitrogen configurations, pyridinic nitrogen (42.3%) dominates MB adsorption by providing Lewis basic edge sites that enable strong electrostatic attraction of the cationic MB molecule, while pyrrolic nitrogen (31.5%) enhances surface wettability through hydrogen bonding, improving MB accessibility to interior micropore adsorption sites. Graphitic nitrogen (20.1%) additionally participates in π–π stacking interactions with the aromatic MB ring system, and oxidized nitrogen (6%) provides supplementary polar sites through dipole–dipole interactions. The collective dominance of pyridinic and pyrrolic nitrogen (73.8%) directly accounts for the chemisorptive nature of MB adsorption and the exceptional capacity of 557.6 mg g^{-1}.

Table 5 Kinetic modelling details

Kinetic model	Differential form	Fitted parameters	Concentration (PPM)		
			20	40	60
Pseudo first order	$\frac{dQ}{dt} = k_1(Q_e - Q_t) \therefore Q_t = Q_e(1 - e^{-k_1 t})$ (ref. 73)	Q_e (mg g^{-1})	225.6	415.2	542.8
		k_1 (min^{-1})	0.14	0.23	0.53
		R^2	0.99	0.98	0.96
Pseudo second order	$\frac{dQ_t}{dt} = k_2(Q_e - Q_t)^2 \therefore Q_t = \frac{k_2 Q_e^2 t}{1 + k_2 Q_e t}$ (ref. 73)	Q_e (mg g^{-1})	265.9	445.6	557.6
		k_2 (g mg min^{-1})	6.3×10^{-4}	9.5×10^{-5}	2.3×10^{-3}
		R^2	0.99	0.99	0.97

The kinetic analysis reveals that the adsorption of MB onto N-TAC is a relatively rapid process dominated by chemisorption mechanisms, with equilibrium being approached within minutes rather than hours.[73] The chemisorption mechanism offers significant practical advantages for water treatment applications. Unlike physical adsorption processes that rely primarily on weak van der Waals forces, the chemisorption mechanism involves stronger interactions between dye molecules and nitrogen-functionalities on the carbon surface, resulting in enhanced selectivity and higher adsorption capacity.[74] This mechanism is particularly beneficial for treating complex wastewater containing multiple contaminants, as the specific chemical interactions favour target dye molecules over competing species. The chemisorption nature also enables effective regeneration of the adsorbent material using 0.1–0.5 M NaOH solution, achieving 95% desorption efficiency by disrupting the electrostatic and hydrogen bonding interactions between dyes and nitrogen sites.[75] The energy requirements for regeneration are relatively low, involving simple pH adjustment and mild heating (60 °C), making the process economically viable for industrial applications.[75]

3.4.2 Isotherm analysis. To investigate the interaction mechanisms between N-TAC and methylene blue solution, isotherm modelling was conducted. Adsorption experiments were performed using N-TAC as the adsorbent across a concentration range from 20 to 150 PPM, as illustrated in Fig. 11(a). The results revealed that significant total dye removal could be effectively achieved up to a concentration of 50 PPM with 10 mg of N-TAC at room temperature. The experimental data, plotted as adsorption capacity (Q_e) against equilibrium concentration (C_e), were fitted to three widely used isotherm models: Langmuir (Fig. 11(b)), Freundlich (Fig. 11(c)), and Temkin (Fig. 11(d)).[73] Table 6 summarizes the parameters obtained from these fittings. The Langmuir isotherm, which describes monolayer adsorption on homogeneous surfaces,[76] yielded a maximum adsorption capacity Q_{max} of 357.4 mg g^{-1}, a binding affinity constant K_L of 7.2 L mg^{-1}, and a correlation coefficient (R^2) of 0.912. This model accounts for surface coverage by balancing the relative rates of adsorption and desorption at dynamic equilibrium, where adsorption is proportional to the available surface area while desorption relates to the covered surface fraction.[73] The high Q_{max} value suggests excellent adsorption capacity, likely attributable to the well-developed surface area and porosity of the N-TAC adsorbent. The Freundlich isotherm, applicable to heterogeneous

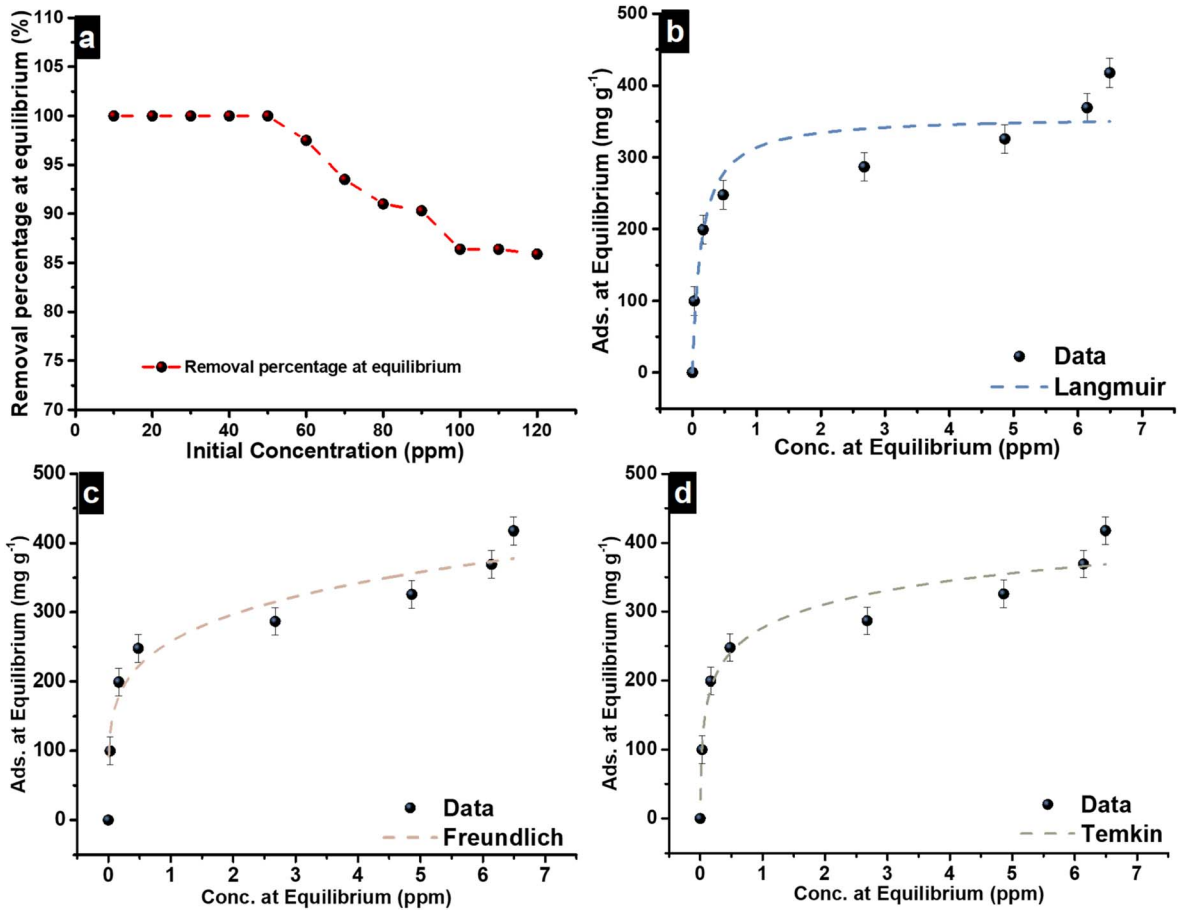

Fig. 11 Adsorption isotherm analysis of N-TAC for methylene blue removal. (a) Equilibrium adsorption capacity (mg g^{-1}) as a function of initial MB concentration (20–150 ppm) at fixed adsorbent dosage of 10 mg in 50 mL solution; isotherm model fits using (b) Langmuir, (c) Freundlich, and (d) Temkin models, with the Temkin isotherm providing the best fit (R^2 = 0.958), indicating heterogeneous chemisorption governed by electrostatic and π–π interactions between MB and nitrogen surface sites.

Table 6 Isotherms modeling details

Isotherm model	Differential form	Fitted parameters	Results at room temp (25 °C)
Langmuir	$\frac{C_e}{Q_e} = \frac{1}{q_m K_e} + \frac{C_e}{q_m}$ (ref. 73)	Q_{max} (mg g^{-1})	357.4
		K_L (L mg^{-1})	7.2
		R^2	0.912
Freundlich	$Q_e = K_F C_e^{1/n}$ (ref. 73)	$K_F\left(\frac{1}{Ln_F mg}1 - \frac{1}{n_F g^{-1}}\right)$	257.5
		n_F (L g^{-1})	0.2047
		R^2	0.911
Temkin	$Q_e = \frac{Rt}{b}\ln K_T + \frac{Rt}{b}\ln C_e$ (ref. 73)	K_T (L g^{-1})	269.5
		b	49.39
		R^2	0.958

surfaces with multilayer adsorption,[75] provided a K_F value of 273.1, an n value of 0.16, and an R^2 of 0.911. The n value below unity indicates favourable adsorption conditions and suggests strong adsorbent–adsorbate interactions even at low equilibrium concentrations.

Most notably, the Temkin isotherm exhibited the best fit (R^2 = 0.958) with binding constant (K_T) of 269.5 L g^{-1} and heat of adsorption constant (b) of 49.39. This model accounts for indirect adsorbate–adsorbate interactions and the linear decrease in adsorption heat with surface coverage. The superior fit suggests that methylene blue adsorption onto N-TAC involves complex interactions beyond simple surface binding, including adsorbate–adsorbate interactions that influence the overall adsorption mechanism.[76]

The exceptional adsorption performance can be attributed to synergistic effects of N-TAC's hierarchical porous architecture, which provides efficient mass transfer pathways, and strategically generated nitrogen functionalities near the carbon surface that create multiple binding sites through electrostatic attractions, π–π interactions, and hydrogen bonding.[71] The predominance of the Temkin model indicates that the nitrogen-doped surface creates a heterogeneous binding environment where adsorbate molecules influence each other's binding behavior, leading to enhanced overall adsorption capacity. These findings, combined with the sustainable nature of the Tondolo shell precursor and cost-effective synthesis approach, position N-TAC as a highly promising adsorbent for advanced water treatment applications. As illustrated in the above-mentioned, the adsorption mechanism of MB on N-TAC is primarily governed by electrostatic attraction, π–π interactions, and hydrogen bonding between the dye molecules and nitrogen/oxygen functional groups on the carbon surface. The negatively charged surface sites interact with the cationic MB through electrostatic forces, while the aromatic domains of the graphitic carbon facilitate π–π stacking. The presence of pyridinic and pyrrolic nitrogen enhances electron density and creates active sites, strengthening the chemisorption process. This is consistent with the pseudo-second-order kinetics and Temkin isotherm fitting, which indicate strong adsorbent–adsorbate interactions and surface heterogeneity.

The adsorption capacity of N-TAC (357 mg g^{-1}) is competitive with several nitrogen-doped activated carbons reported in the literature for methylene blue removal (Table 7), outperforming materials such as nitrogen-doped hydrochar (57.52 mg g^{-1}) and sludge-derived nitrogen-doped carbon (35.83 mg g^{-1}), while remaining below higher-performing materials including bamboo-derived nitrogen self-doped activated carbon (458 mg g^{-1}) and nitrogen/oxygen co-doped honeycomb porous carbons (631 mg g^{-1}), differences attributable to precursor type, activation strategy, and pore structure development. The Langmuir isotherm best described the adsorption equilibrium of N-TAC, confirming monolayer adsorption on homogeneous active sites, and collectively these results highlight the important role of nitrogen functionalities and developed porosity in enhancing methylene blue uptake.

3.4.3 Practical considerations, scalability, and future directions potential. While this study focuses on single-dye adsorption under controlled conditions, real wastewater scenarios present more complex challenges. In actual textile wastewater, N-TAC would encounter multiple competing pollutants (various dyes, heavy metals, organic compounds), high ionic strength (0.1–1.0 M dissolved salts), and pH variations (6–10), which could reduce adsorption efficiency by 20–30% through competitive binding and electrostatic screening effects. Surfactants and organic additives commonly present in industrial wastewater may further compete for active sites or form complexes that hinder dye–adsorbent interactions. Despite these challenges, the robust nitrogen-doped structure and demonstrated selectivity suggest N-TAC could maintain reasonable performance (estimated 70–80% of laboratory values) in real wastewater with appropriate pretreatment. Future work should explore integrated adsorption-degradation strategies for total mineralization: coupling N-TAC with advanced oxidation processes (Fenton, persulfate) as dual adsorbent-catalyst support, photocatalytic functionalization with TiO_2 or g-C_3N_4 for simultaneous adsorption and light-driven degradation, electrochemical oxidation leveraging N-TAC's demonstrated electroactivity, or bioaugmentation using spent adsorbent as microbial support.[86] These hybrid approaches would transform N-TAC into a multifunctional platform addressing industrial wastewater through synergistic pollutant removal and destruction mechanisms beyond separation alone.

Preliminary cost analysis reveals N-TAC production costs are approximately 40% lower than commercial activated carbon due

Table 7 Adsorption performance comparison of N-TAC with reported nitrogen-doped porous carbons for methylene blue (MB) removal

Adsorbent	Precursor/Source	Dopant/Modification	Maximum adsorption capacity (mg g^{-1})	Initial MB concentration (mg L^{-1})	Best isotherm model	Ref
BSNC-800-4	Bamboo shoots	Self-N-doping	458	500	Langmuir	75
HPC-3 porous carbon	Coal tar pitch	N,O co-doping (melamine sponge)	631.0	50–150	Langmuir	77
PB-700-1 biochar	Bamboo	Urea N-doping	499.3	—	Langmuir	30
N,S-PCSs-1	Glucose	N,S co-doping (L-cysteine)	909.10	—	Langmuir	73
AC-N mesoporous carbon	Cypress AC	Urea N-doping	910.95	—	Langmuir	71
GPC-N activated carbon	*Lycium chinensis* stalk	NH_4Cl N-doping	496.53	10	Langmuir	78
PCM-K porous carbon	Pine nut shell	N-doping + activation	766.9	50–500	Langmuir	79
N-doped AC	Polish brown coal	Urea modification	350	0–200	Freundlich	80
CQDs/HMS composite	Histidine & cysteine	N,S-doped carbon QDs	370.4	20–300	Langmuir	81
Carbon-ZD	ZIF-derived carbon	N-doped porous carbon	1148.2	600	Langmuir	82
Bagasse biochar	Bagasse biomass	Urea N-doping + $NaHCO_3$ activation	84.2	30	Freundlich	83
N-doped hydrochar	Biomass + N-rich wastewater	Urea/melamine/ NH_4Cl	57.52	≤300	Freundlich	84
N-doped sludge carbon	Excess sludge	Urea N-doping	35.83	50	Langmuir	85
N-TAC	This work	N-doped activated carbon	357	20–150	Langmuir	This work

to abundant agricultural waste utilization and single pyrolysis step synthesis protocols. Main costs include energy consumption during pyrolysis and nitrogen precursor costs. Scale-up challenges include managing high activation energy requirements (700 °C), safe nitrogen precursor handling, and maintaining consistent quality across batches. Solutions involve continuous pyrolysis systems with heat recovery, automated feeding systems, and real-time quality monitoring. Environmental benefits include waste valorisation, reduced landfill burden, and lower carbon footprint compared to fossil-based activated carbon.

4. Conclusion

This work demonstrates the successful transformation of Tondolo agricultural waste into a high-performance nitrogen-doped activated carbon (N-TAC) through K_2CO_3 activation, yielding a hierarchically porous material with a specific surface area of 3504.5 m^2 g^{-1} where pyridinic, pyrrolic, and graphitic nitrogen functionalities proved decisive in simultaneously enhancing energy storage and water remediation performance. Three-electrode characterization in 1 M $NaNO_3$ confirmed a synergistic coexistence of EDLC and pseudocapacitive mechanisms, with power law analysis, Trasatti deconvolution, and Dunn's method collectively establishing surface-controlled charge storage contributions of 63–71%, while asymmetric *b*-value distributions confirmed potential-dependent charge storage behavior across both electrode windows. Trasatti analysis precisely quantified electrode-specific contributions, with the negative electrode demonstrating superior performance over the positive electrode, driven by favorable Na^+ accessibility and nitrogen-mediated redox activity under cathodic polarization, while EIS confirmed fast charge transfer kinetics (ESR = 2.05 Ω, R_{CT} = 2.75 Ω, τ = 0.87 s). The assembled symmetric device delivered 12.1 Wh kg^{-1} with 94% capacitance retention over 10 000 cycles, while for water remediation N-TAC achieved 99.9% methylene blue removal at 50 ppm with an adsorption capacity of 557.6 mg g^{-1}, governed by chemisorption through electrostatic and π–π interactions, best described by pseudo-second-order kinetics (R^2 = 0.97) and the Temkin isotherm (R^2 = 0.958). These findings position N-TAC at the forefront of sustainable multifunctional carbon materials for the water–energy nexus, with future perspectives encompassing binder-free electrode fabrication, green membrane development, electrochemical degradation integration, and regenerable architectures for scalable long-term environmental and energy applications.

Conflicts of interest

There are no conflicts to declare.

Data availability

The datasets generated and analyzed during this study are included in this published article and its supplementary information (SI) files. Additional datasets are available from the corresponding author upon reasonable request. Supplementary information: detailed electrochemical characterization and performance evaluation of nitrogen-doped activated carbons derived from waste fruit

peels (N-TAC) for both supercapacitor applications and water treatment. It includes three-electrode measurements (cyclic voltammetry and galvanostatic charge–discharge), power-law analysis of charge storage mechanisms, Trasatti's method for quantifying EDLC and pseudocapacitive contributions, and Dunn's method for current separation (Fig. S1–S4). Post-cycling EIS and SEM analysis are presented in Fig. S5, while Fig. S6 and S7 demonstrate N-TAC's water purification performance through methylene blue adsorption studies, including calibration curves and UV-vis spectra at varying concentrations and time intervals. See DOI: https://doi.org/10.1039/d6ra02137a.

Acknowledgements

Financial support was provided by the NRF South African (Grant PSTD240130203302), and the NRF South African Research Chairs Initiative (SARChI)-University of Pretoria co-funded chair (Grant RNEWSW240307208354). Likewise, funding from the University of South Africa & iThemba LABS-NRF was provided to the UNESCO-UNISA-ITLABS/NRF Africa Chair in Nanosciences & Nanotechnology (Grant U2ACN2-2018/2025). The ideas, findings, conclusions, and recommendations expressed in this publication are those of the author(s) and do not necessarily reflect the views of the NRF, which accepts no liability in this regard. The authors gratefully acknowledge the National Research Foundation (NRF), iThemba LABS, the UNESCO-UNISA Chair, and the Institut National de la Recherche Scientifique Canada (INRS) for providing access to laboratories and for their characterisations. During the preparation of this work the author(s) used Claude (an AI assistant by Anthropic) to improve clarity, check grammar, and refine the language of the manuscript. After using this tool/service, the author(s) reviewed and edited the content as needed and take(s) full responsibility for the content of the published article.

References

1 V. N. Kitenge, T. Baloyi, N. Diop, H. E. A. Mohamed, N. Botha, S. Thior, A. ShamsKhameneh, I. Madiba, N. Manyala, M. Chaker, *et al.*, Interface engineering of activated carbon *via* nitrogen and nitrogen-sulfur doping for high-performance supercapacitors and dye adsorption, *J. Environ. Chem. Eng.*, 2026, **14**(1), 120693, DOI: 10.1016/j.jece.2025.120693.

2 D. C. C. da Silva Medeiros, M. Usman, P. Chelme-Ayala and M. Gamal El-Din, Biochar-enhanced removal of naphthenic acids from oil sands process water: Influence of feedstock and chemical activation, *Energy Environ. Sustainability*, 2025, **1**(2), 100028, DOI: 10.1016/j.eesus.2025.100028.

3 V. N. Kitenge and N. Manyala, Tailoring Porosity and Surface Chemistry of Biomass-Derived Activated Carbon *via* Nitrogen and Nitrogen-Sulfur Doping for Supercapacitors Application, *ECS*, 2025, (10), 3425, DOI: 10.1149/MA2025-02103425mtgabs.

4 L. Li, Y.-F. Ren, C.-W. Shao, L.-Y. Zhang, G.-R. Qi, X.-S. Cong, X.-Y. Wei, Z.-C. Fan and X.-Y. Zhang, Unlocking a new application of coal and biomass co-ethanolysis: high-performance supercapacitor based on N/O self-doped hierarchical porous carbons, *Fuel*, 2026, **406**, 137164, DOI: 10.1016/j.fuel.2025.137164.

5 M. R. Thalji, A. Al Mahmud, F. Mahmoudi, A. H. Mady, D. R. Kumar, K. F. Chong, C. Park and J.-J. Shim, Ethyl xanthate-driven *in situ* synthesis of Ni-Fe sulfide@Ti3C2Tx MXene hybrid electrodes for ultra-high-performance supercapacitors, *Chem. Eng. J.*, 2025, **522**, 167789, DOI: 10.1016/j.cej.2025.167789.

6 J. Guo, Y. Gao, X. Cao, L. Li, X. Yu, S. Chi, H. Liu, G. Tian and X. Zhao, Ni/N co-doped NH2-MIL-88(Fe) derived porous carbon as an efficient electrocatalyst for methanol and water co-electrolysis, *Renewable Energy*, 2025, **244**, 122661, DOI: 10.1016/j.renene.2025.122661.

7 A. M. Abioye and F. N. Ani, Recent development in the production of activated carbon electrodes from agricultural waste biomass for supercapacitors: A review, *Renewable Sustainable Energy Rev.*, 2015, **52**, 1282–1293, DOI: 10.1016/j.rser.2015.07.129.

8 D. Y. Koseoglu-Imer, H. V. Oral, C. S. Coutinho Calheiros, P. Krzeminski, S. Güçlü, S. A. Pereira, J. Surmacz-Górska, E. Plaza, P. Samaras, P. M. Binder, *et al.*, Current challenges and future perspectives for the full circular economy of water in European countries, *J. Environ. Manage.*, 2023, **345**, 118627, DOI: 10.1016/j.jenvman.2023.118627.

9 V. Kitenge, D. Tarimo, k. Oyedotun, G. Rutavi and N. Manyala, Facile and sustainable technique to produce low-cost high surface area mangosteen shell activated carbon for supercapacitors applications, *J. Energy Storage*, 2022, **56**, 105876. https://worldcat.org/z-wcorg/.

10 D. J. Tarimo, K. Oyedotun, A. Mirghni, G. Rutavi, V. N. Kitenge and N. Manyala, Recycling of biomass wastes from amarula husk by a modified facile economical water salt method for high energy density ultracapacitor application, *J. Energy Storage*, 2022, **53**, 105166.

11 Y. Wang, Y. Wang, L. Zhang, X. Tang, J. Ai, D. Xiao and Q. Zhao, Exogenous phosphorus supplementation and sodium reduction treatment to realize N, P co-doped hard carbon with reduced oxygen-containing groups for high-performance sodium-ion batteries, *J. Power Sources*, 2025, **630**, 236156, DOI: 10.1016/j.jpowsour.2024.236156.

12 S. Zhu, J. Xu, J. Xie, Z. Zhang, Q. Ding and K. Chen, Ultrafast dyeing wastewater purification by high-performance and reusable lignin-derived activated porous carbon filter, *Sep. Purif. Technol.*, 2024, **349**, 127672.

13 X. Yang, Y. Xie, X. Zheng, J. Gai, Y. Zhao, Q. Zhang and H. Yan, Enhancing electrochemical performance of CNTs-decorated K3V3(PO4)4@C nanocomposite *via* Nd3+-doping for advanced potassium energy storage, *Ceram. Int.*, 2026, **52**(4), 4997–5005, DOI: 10.1016/j.ceramint.2025.12.274.

14 V. N. Kitenge, D. J. Tarimo, G. Rutavi, V. M. Maphiri, S. Sarr, M. Diop, M. Chaker and N. Manyala, Influence of nitrogen and sulfur co-doped activated carbon used as electrode material in EmiFSI ionic liquid toward high-energy supercapacitors, *J. Energy Storage*, 2024, **81**, 110453, DOI: 10.1016/j.est.2024.110453.

15 Y. S. Al-Degs, M. I. El-Barghouthi, M. A. Khraisheh, M. N. Ahmad and S. J. Allen, Effect of Surface Area, Micropores, Secondary Micropores, and Mesopores Volumes of Activated Carbons on Reactive Dyes Adsorption from Solution, *Sep. Sci. Technol.*, 2005, **39**(1), 97–111, DOI: 10.1081/ss-120027403.

16 R.-L. Tseng, S.-K. Tseng, F.-C. Wu, C.-C. Hu and C.-C. Wang, Effects of micropore development on the physicochemical properties of KOH-activated carbons, *J. Chin. Inst. Chem. Eng.*, 2008, **39**(1), 37–47.

17 O. Fasakin, J. K. Dangbegnon, D. Y. Momodu, M. J. Madito, K. O. Oyedotun, M. A. Eleruja and N. Manyala, Synthesis and characterization of porous carbon derived from activated banana peels with hierarchical porosity for improved electrochemical performance, *Electrochim. Acta*, 2018, **262**, 187–196, DOI: 10.1016/j.electacta.2018.01.028.

18 Q. Wei, Z. Chen, Y. Cheng, X. Wang, X. Yang and Z. Wang, Preparation and electrochemical performance of orange peel based-activated carbons activated by different activators, *Colloids Surf., A*, 2019, **574**, 221–227.

19 C. Palma, L. Lloret, A. Puen, M. Tobar and E. Contreras, Production of carbonaceous material from avocado peel for its application as alternative adsorbent for dyes removal, *Chin. J. Chem. Eng.*, 2016, **24**(4), 521–528.

20 V. Kitenge, D. Tarimo, K. Oyedotun, G. Rutavi, D. Bakhoum and N. Manyala, Electrical Double-Layer Capacitor Based on Low Aqueous Electrolyte Contents in EmimTFO Ionic Liquid, *Int. J. Energy Res.*, 2023, **2023**(1), 8659009.

21 S. Thior, V. Kitenge, K. O. Otun, R. A. Adam, N. F. Diop, B. D. Ngom and N. Manyala, Influence of water-in-salt electrolytes on the electrochemical performance of porous N and S co-doped carbon electrodes in supercapacitors, *New J. Chem.*, 2025, 2129–2142.

22 N. F. Sylla, N. M. Ndiaye, B. D. Ngomb, B. K. Mutuma, D. Momodu, M. Chaker and N. Manyala, Ex-situ nitrogen-doped porous carbons as electrode materials for high performance supercapacitor, *J. Colloid Interface Sci.*, 2020, **569**, 332. https://worldcat.org/z-wcorg/.

23 V. Kitenge, A. Shams Khameneh, S. Heshmatian, N. Matinise, N. Botha, I. Madiba, N. Manyala and M. Maaza, Walnut-shell-derived porous carbon for efficient room-temperature adsorption of organic dyes, *Sci. Rep.*, 2026, **16**, 9756, DOI: 10.1038/s41598-026-38102-9.

24 D. R. Lobato-Peralta, H. O. Orugba, D. Arias, P. Sebastian, J. A. Okolie and P. U. Okoye, Optimizing pre-carbonization temperature in sustainable cow hoof-derived activated carbon for high-performance supercapacitor electrodes, *Surf. Interfaces*, 2025, **56**, 105701.

25 R. A. Adam, D. J. Tarimo, V. M. Maphiri, A. A. Mirghni, O. Fasakin and N. Manyala, Effects of the physisorption properties of human hair-derived activated carbon as a potential electrode for symmetric supercapacitor, *Mater. Renew. Sustain. Energy*, 2025, **14**(1), 22.

26 J. d. D. M. Ufitikirezi, M. Filip, M. Ghorbani, T. Zoubek, P. Olšan, R. Bumbálek, M. Strob, P. Bartoš, S. N. Umurungi and Y. T. Murindangabo, Agricultural waste valorization: exploring environmentally friendly approaches to bioenergy conversion, *Sustainability*, 2024, **16**(9), 3617.

27 S. Thior, V. N. Kitenge, N. F. Diop, K. O. Otun, V. M. Maphiri, R. A. M. Adam, B. D. Ngom and N. Manyala, Enhancing potential window with ionic liquid/water in salt mixture in co-doped activated carbon electrodes for high-energy supercapacitors, *J. Energy Storage*, 2026, **141**, 119425, DOI: 10.1016/j.est.2025.119425.

28 O. P. Nanda and S. Badhulika, Biomass derived Nitrogen, Sulphur, and Phosphorus self-doped micro-meso porous carbon for high-energy symmetric supercapacitor – With a detailed study of the effect of different current collectors, *J. Energy Storage*, 2022, **56**, 106042, DOI: 10.1016/j.est.2022.106042.

29 Y. Zheng, Y. Liu, X. Guo, Z. Chen, W. Zhang, Y. Wang, X. Tang, Y. Zhang and Y. Zhao, Sulfur-doped g-C3N4/rGO porous nanosheets for highly efficient photocatalytic degradation of refractory contaminants, *J. Mater. Sci. Technol.*, 2020, **41**, 117–126, DOI: 10.1016/j.jmst.2019.09.018.

30 Z. Li, B. Xing, Y. Ding, Y. Li and S. Wang, A high-performance biochar produced from bamboo pyrolysis with in-situ nitrogen doping and activation for adsorption of phenol and methylene blue, *Chin. J. Chem. Eng.*, 2020, **28**(11), 2872–2880.

31 Q. Zhou, Z. Liu, X. Wang, Y. Li, X. Qin, L. Guo, L. Zhou and W. Xu, Co3S4-pyrolysis lotus fiber flexible textile as a hybrid electrocatalyst for overall water splitting, *J. Energy Chem.*, 2024, **89**, 336–344, DOI: 10.1016/j.jechem.2023.10.015.

32 J. Y. Lu, Z. Q. Bu, Y. Q. Lei, D. Wang, B. He, J. Wang and W. T. Huang, Facile microwave-assisted synthesis of Sb2O3-CuO nanocomposites for catalytic degradation of p-nitrophenol, *J. Mol. Liq.*, 2024, **409**, 125503, DOI: 10.1016/j.molliq.2024.125503.

33 C. M. Ashande, F. L. Lukoki, D. D. Tshilanda, D. Tshibangu and P. T. Mpiana, A mini review on the phytochemistry and pharmacology of Aframomum alboviolaceum (zingiberaceae), *South Asian Res. J. Nat. Proc*, 2021, **4**, 24–35.

34 B. E. Conway, *Electrochemical Supercapacitors: Scientific Fundamentals and Technological Applications*, Springer Science + Business Media, LLC, 1999, DOI: 10.1007/978-1-4757-3058-6.

35 S. Vaquero, J. Palma, M. Anderson and R. Marcilla, Mass-Balancing of Electrodes as a Strategy to Widen the Operating Voltage Window of Carbon/Carbon Supercapacitors in Neutral Aqueous Electrolytes, *Int. J. Electrochem. Sci.*, 2013, **8**(8), 10293–10307, DOI: 10.1016/S1452-3981(23)13111-7.

36 V. N. Kitenge, K. O. Oyedotun, O. Fasakin, D. J. Tarimo, N. F. Sylla, X. Van Heerden and N. Manyala, Enhancing the electrochemical properties of a nickel–cobalt-manganese ternary hydroxide electrode using graphene foam for supercapacitors applications, *Mater. Renew. Sustain. Energy*, 2021, **10**(1), 7, DOI: 10.1007/s40243-021-00192-y.

37 D. F. Swinehart, The beer-lambert law, *J. Chem. Educ.*, 1962, **39**(7), 333.

38 N. F. Diop, K. O. Otun, S. Thior, V. M. Maphiri, V. N. Kitenge, S. Sarr, N. F. Sylla, X. Wenqiang, M. Chaker, B. D. Ngom, *et al.*, Facile room-temperature solution-phase synthesis of a ZIF-67 : Ni hybrid-MOF battery type material for supercapacitor applications, *RSC Adv.*, 2025, **15**(42), 34976–34990, DOI: 10.1039/d5ra05741h.

39 C. Schneidermann, N. Jäckel, S. Oswald, L. Giebeler, V. Presser and L. Borchardt, Solvent-Free Mechanochemical Synthesis of Nitrogen-Doped Nanoporous Carbon for Electrochemical Energy Storage, *Chemsuschem*, 2017, **10**(11), 2416–2424, DOI: 10.1002/cssc.201700459.

40 Y. Zhang, L. Liu, P. Zhang, J. Wang, M. Xu, Q. Deng, Z. Zeng and S. Deng, Ultra-high surface area and nitrogen-rich porous carbons prepared by a low-temperature activation method with superior gas selective adsorption and outstanding supercapacitance performance, *Chem. Eng. J.*, 2019, **355**, 309–319, DOI: 10.1016/j.cej.2018.08.169.

41 Y. Dai, S. He, L. Yu, J. Liu, L. Gan and M. Long, One-step preparation of nitrogen-doped porous carbons with excellent properties for high-performance supercapacitors, *J. Phys. Chem. Solids*, 2019, **129**, 122–127, DOI: 10.1016/j.jpcs.2018.12.043.

42 T. K. Das, S. Banerjee, A. Kumar, A. K. Patra, P. U. Sastry, A. K. Debnath and V. Sudarsan, Nitrogen-doped hierarchically porous carbon obtained *via* single step method for high performance supercapacitors, *Int. J. Hydrogen Energy*, 2022, **47**(26), 12829–12840, DOI: 10.1016/j.ijhydene.2022.02.036.

43 K. Li, W. Chen, H. Yang, Y. Chen, S. Xia, M. Xia, X. Tu and H. Chen, Mechanism of biomass activation and ammonia modification for nitrogen-doped porous carbon materials, *Bioresour. Technol.*, 2019, **280**, 260–268, DOI: 10.1016/j.biortech.2019.02.039.

44 D. Liu, Y. Liu, Y. Ding and B. Fan, Preparation of N/O co-doped porous carbon by a one-step activation method for supercapacitor electrode materials, *RSC Adv.*, 2022, **12**(32), 20866–20875, DOI: 10.1039/D2RA02732A.

45 W. Ruan, Y. Wang, C. Liu, D. Xu, P. Hu, Y. Ye, D. Wang, Y. Liu, Z. Zheng and D. Wang, One-step fabrication of N-doped activated carbon by NH3 activation coupled with air oxidation for supercapacitor and CO2 capture applications, *J. Anal. Appl. Pyrolysis*, 2022, **168**, 105710, DOI: 10.1016/j.jaap.2022.105710.

46 L.-Y. Meng and S.-J. Park, One-pot synthetic method to prepare highly N-doped nanoporous carbons for CO2 adsorption, *Mater. Chem. Phys.*, 2014, **143**(3), 1158–1163, DOI: 10.1016/j.matchemphys.2013.11.016.

47 Z. Geng, Q. Xiao, H. Lv, B. Li, H. Wu, Y. Lu and C. Zhang, One-Step Synthesis of Microporous Carbon Monoliths Derived from Biomass with High Nitrogen Doping Content for Highly Selective CO2 Capture, *Sci. Rep.*, 2016, **6**(1), 30049, DOI: 10.1038/srep30049.

48 S. He, G. Chen, H. Xiao, G. Shi, C. Ruan, Y. Ma, H. Dai, B. Yuan, X. Chen and X. Yang, Facile preparation of N-doped activated carbon produced from rice husk for CO2 capture, *J. Colloid Interface Sci.*, 2021, **582**, 90–101, DOI: 10.1016/j.jcis.2020.08.021.

49 G. Singh, I. Y. Kim, K. S. Lakhi, P. Srivastava, R. Naidu and A. Vinu, Single step synthesis of activated bio-carbons with a high surface area and their excellent CO2 adsorption capacity, *Carbon*, 2017, **116**, 448–455, DOI: 10.1016/j.carbon.2017.02.015.

50 R. Cong, H. H. Park, M. Jo, H. Lee and C. S. Lee, Synthesis and Electrochemical Performance of Electrostatic Self-Assembled Nano-Silicon@N-Doped Reduced Graphene Oxide/Carbon Nanofibers Composite as Anode Material for Lithium-Ion Batteries, *Molecules*, 2021, 4831, DOI: 10.20944/preprints202106.0411.v1.

51 J. Zhao, C. Liu, K. Xiang, Q. Cheng, Y. Li, H. Lin, K. T. Lee, L. An, S. Tang, Y. C. Cao, *et al.*, *In-Situ* Template Formation Strategy for the Preparation of Nitrogen Doped Carbon Nanocage With Graphitic Shell as Electrode Material for Supercapacitor, *J. Nanosci. Nanotechnol.*, 2018, **18**(10), 6949–6956, DOI: 10.1166/jnn.2018.15454.

52 A. Sadezky, H. Muckenhuber, H. Grothe, R. Niessner and U. Pöschl, Raman microspectroscopy of soot and related carbonaceous materials: Spectral analysis and structural information, *Carbon*, 2005, **43**(8), 1731–1742, DOI: 10.1016/j.carbon.2005.02.018.

53 S. Holmberg, M. Ghazinejad, E. Cho, D. George, B. Pollack, A. Perebikovsky, R. Ragan and M. Madou, Stress-Activated Pyrolytic Carbon Nanofibers for Electrochemical Platforms, *Electrochim. Acta*, 2018, **290**, 639–648, DOI: 10.1016/j.electacta.2018.09.013.

54 X. Zhang, R. Zhang, T. Kang, Y. Hu and C. Li, Experimental and Mechanistic Research on Methane Adsorption in Anthracite Modified by Electrochemical Treatment Using Selected Electrode Materials, *Sci. Rep.*, 2019, **9**(1), 17163, DOI: 10.1038/s41598-019-53840-9.

55 N. Chaiammart, A. Taechamahaphan, P. Chakartnarodom, W. Prakaypan, T. Ishizaki, A. Eiad-ua and G. Panomsuwan, Valorization of Macadamia Nut Shell Waste into Activated Carbons for Electrochemical Supercapacitor Electrodes, *ACS Omega*, 2026, **11**, 13036–13051, DOI: 10.1021/acsomega.5c06396.

56 F. Béguin, V. Presser, A. Balducci and E. Frackowiak, Carbons and Electrolytes for Advanced Supercapacitors, *Adv. Mater.*, 2014, **26**(14), 2219–2251, DOI: 10.1002/adma.201304137.

57 S. Fleischmann, J. B. Mitchell, R. Wang, C. Zhan, D.-e. Jiang, V. Presser and V. Augustyn, Pseudocapacitance: from fundamental understanding to high power energy storage materials, *Chem. Rev.*, 2020, **120**(14), 6738–6782.

58 K. O. Oyedotun, F. Barzegar, A. A. Mirghni, A. A. Khaleed, T. M. Masikhwa and N. Manyala, Examination of High-Porosity Activated Carbon Obtained from Dehydration of White Sugar for Electrochemical Capacitor Applications, *ACS Sustain. Chem. Eng.*, 2019, **7**(1), 537–546, DOI: 10.1021/acssuschemeng.8b04080.

59 G. Rutavi, D. J. Tarimo, V. M. Maphiri, V. N. Kitenge and N. Manyala, Exploration of metal-layered double hydroxide composite material for hybrid capacitor produced by facile

and efficient electrodeposition process, *J. Alloys Compd.*, 2022, **929**, 167216, DOI: 10.1016/j.jallcom.2022.167216.

60 G. Rutavi, D. J. Tarimo, V. M. Maphiri, V. N. Kitenge and N. Manyala, Assessment of the electrodeposition synthesized manganese chromite and cobalt-nickel layered double hydroxide composite for high-performance supercapacitor applications, *J. Energy Storage*, 2023, **58**, 106442.

61 D. Dong, Y. Zhang, Y. Xiao, T. Wang, J. Wang, C. E. Romero and W.-p. Pan, High performance aqueous supercapacitor based on nitrogen-doped coal-based activated carbon electrode materials, *J. Colloid Interface Sci.*, 2020, **580**, 77–87.

62 N. Venkatesan, T. Kesavan, M. Raja, K. Ramanujam and N. N. Fathima, Efficient electrochemical performance of nitrogen-doped porous activated carbon for high energy symmetric pouch cell supercapacitors, *J. Energy Storage*, 2022, **55**, 105698, DOI: 10.1016/j.est.2022.105698.

63 X. Han, H. Jiang, Y. Zhou, W. Hong, Y. Zhou, P. Gao, R. Ding and E. Liu, A high performance nitrogen-doped porous activated carbon for supercapacitor derived from pueraria, *J. Alloys Compd.*, 2018, **744**, 544–551.

64 W. Wang, H. Quan, W. Gao, R. Zou, D. Chen, Y. Dong and L. Guo, N-Doped hierarchical porous carbon from waste boat-fruited sterculia seed for high performance supercapacitors, *RSC Adv.*, 2017, 7(27), 16678–16687.

65 J. Cui, Z.-X. Zhang, H. Quan, Y. Hu, S. Wang and D. Chen, Effect of various ammonium salts as activating additive on the capacitance performance of hierarchical porous carbon derived from camellia husk, *J. Energy Storage*, 2022, **51**, 104347.

66 Z. Xu, Y. Li, D. Li, D. Wang, J. Zhao, Z. Wang, M. N. Banis, Y. Hu and H. Zhang, N-enriched multilayered porous carbon derived from natural casings for high-performance supercapacitors, *Appl. Surf. Sci.*, 2018, **444**, 661–671.

67 F. Miao, C. Shao, X. Li, K. Wang, N. Lu and Y. Liu, Three-dimensional freestanding hierarchically porous carbon materials as binder-free electrodes for supercapacitors: high capacitive property and long-term cycling stability, *J. Mater. Chem. A*, 2016, **4**(15), 5623–5631.

68 D. Guo, R. Xin, Z. Zhang, W. Jiang, G. Hu and M. Fan, N-doped hierarchically micro-and mesoporous carbons with superior performance in supercapacitors, *Electrochim. Acta*, 2018, **291**, 103–113.

69 D. Guo, R. Xin, Y. Wang, W. Jiang, Q. Gao, G. Hu and M. Fan, N-doped carbons with hierarchically micro-and mesoporous structure derived from sawdust for high performance supercapacitors, *Microporous Mesoporous Mater.*, 2019, **279**, 323–333.

70 Z. Ma, W. Wang, Q. Bai, F. Zhou, C. Ma and Y. Shen, Three-dimensional nitrogen-doping hierarchically porous carbon derived from polyacrylamide-lignocellulose aerogel for high energy density supercapacitors, *J. Power Sources*, 2025, **631**, 236304, DOI: 10.1016/j.jpowsour.2025.236304.

71 C. Yao, M. Wang, W. Jiang and Y. Chen, Study on a novel N-doped mesoporous carbon for the efficient removal of methylene blue from aqueous solution, *Environ. Eng. Res.*, 2021, **26**(5), DOI: 10.4491/eer.2020.339.

72 R. N. Kasavo, M. Bhaumik and H. G. Brink, Removal of chromium from aqueous solution using a nanocomposite of nickel ferrite and polyaniline doped with 2-naphthalene sulfonic acid, *J. Environ. Chem. Eng.*, 2023, **11**(6), 111229.

73 Y. Ren, F. Chen, K. Pan, Y. Zhao, L. Ma and S. Wei, Studies on kinetics, isotherms, thermodynamics and adsorption mechanism of methylene blue by N and S co-doped porous carbon spheres, *Nanomaterials*, 2021, **11**(7), 1819.

74 T. H. Tran, H. H. Le, T. H. Pham, D. T. Nguyen, D. D. La, S. W. Chang, S. M. Lee, W. J. Chung and D. D. Nguyen, Comparative study on methylene blue adsorption behavior of coffee husk-derived activated carbon materials prepared using hydrothermal and soaking methods, *J. Environ. Chem. Eng.*, 2021, **9**(4), 105362, DOI: 10.1016/j.jece.2021.105362.

75 B. Mi, J. Wang, H. Xiang, F. Liang, J. Yang, Z. Feng, T. Zhang, W. Hu, X. Liu and Z. Liu, Nitrogen self-doped activated carbons derived from bamboo shoots as adsorbent for methylene blue adsorption, *Molecules*, 2019, **24**(16), 3012.

76 I. Tan, B. Hameed and A. Ahmad, Equilibrium and kinetic studies on basic dye adsorption by oil palm fibre activated carbon, *Chem. Eng. J.*, 2007, **127**(1–3), 111–119.

77 Q.-Q. Zhuang, J.-P. Cao, Y. Wu, M. Zhao, X.-Y. Zhao, Y.-P. Zhao and H.-C. Bai, Heteroatom nitrogen and oxygen co-doped three-dimensional honeycomb porous carbons for methylene blue efficient removal, *Appl. Surf. Sci.*, 2021, **546**, 149139.

78 Y. Ren, W. Geng, R. Xu, P. Wang and H. Zhao, Tuning electronic and pore structures of biochar *via* nitrogen and magnesium doping for superior methylene blue adsorption: synergistic mechanisms and kinetic analysis, *ACS Omega*, 2025, **10**(29), 31679–31692.

79 L. Lv, Y. Huang and D. Cao, Nitrogen-doped porous carbons with ultrahigh specific surface area as bifunctional materials for dye removal of wastewater and supercapacitors, *Appl. Surf. Sci.*, 2018, **456**, 184–194.

80 J. Kaźmierczak-Raźna, P. Półrolniczak, K. Wasiński, R. Pietrzak and P. Nowicki, Comparison of physicochemical, sorption and electrochemical properties of nitrogen-doped activated carbons obtained with the use of microwave and conventional heating, *Adsorption*, 2019, **25**(3), 405–417.

81 T. Teymoorian, N. Hashemi, M. H. Mousazadeh and Z. N. Entezarian, S doped carbon quantum dots inside mesoporous silica for effective adsorption of methylene blue dye, *SN Appl. Sci.*, 2021, **3**(3), 305.

82 S. Xu, Y. Lv, X. Zeng and D. Cao, ZIF-derived nitrogen-doped porous carbons as highly efficient adsorbents for removal of organic compounds from wastewater, *Chem. Eng. J.*, 2017, **323**, 502–511.

83 F. Cai, C. Li, C. Yang, Y. Wang, H. Zhou, S. Yang, J. Tang, L. Wang and Y. Liu, Preparation of nitrogen-doped bagasse-derived biochar with outstanding methylene blue adsorption performance, *Ind. Crops Prod.*, 2025, **224**, 120415.

84 Z. Lin, R. Wang, S. Tan, K. Zhang, Q. Yin, Z. Zhao and P. Gao, Nitrogen-doped hydrochar prepared by biomass and nitrogen-containing wastewater for dye adsorption: effect

of nitrogen source in wastewater on the adsorption performance of hydrochar, *J. Environ. Manage.*, 2023, **334**, 117503.

85 W. Hu, Y. Xie, S. Lu, P. Li, T. Xie, Y. Zhang and Y. Wang, One-step synthesis of nitrogen-doped sludge carbon as a bifunctional material for the adsorption and catalytic oxidation of organic pollutants, *Sci. Total Environ.*, 2019, **680**, 51–60.

86 Y. Chen, X. Zhao, J. Zhang, H. Wang, Z. Ye, W. Ma, R. Mao, S. Zhang, R. A. Dahlgren, H. Gao, *et al.*, Combined application of nitrate and schwertmannite promotes As(III) immobilization and greenhouse gas emission reduction in flooded paddy fields, *J. Environ. Chem. Eng.*, 2025, **13**(6), 119845, DOI: 10.1016/j.jece.2025.119845.